# IMITATION OF RADIOFREQUENCY ABLATION WITH FIBER DELIVERED LASER SYSTEM FOR MAGNETIC RESONANCE GUIDED TREATMENT OF ATRIAL FIBRILLATION

A THESIS
SUBMITTED TO THE DEPARTMENT OF ELECTRICAL
AND
ELECTRONICS ENGINEERING
AND THE INSTITUTE OF ENGINEERING AND SCIENCE
OF BILKENT UNIVERSITY
IN PARTIAL FULFILLMENT OF THE REQUIREMENTS
FOR THE DEGREE OF
MASTER OF SCIENCE

By

M. Can KERSE

January, 2010

I certify that I have read this thesis and that in my opinion it is fully adequate, in scope and in quality, as a thesis for the degree of Master of Science.

Prof. Dr. Ergin Atalar (Supervisor)

I certify that I have read this thesis and that in my opinion it is fully adequate, in scope and in quality, as a thesis for the degree of Master of Science.

Asst. Prof. Dr. F. Ömer İlday (Co. Supervisor)

I certify that I have read this thesis and that in my opinion it is fully adequate, in scope and in quality, as a thesis for the degree of Master of Science.

Prof. Dr. Orhan Aytür

I certify that I have read this thesis and that in my opinion it is fully adequate, in scope and in quality, as a thesis for the degree of Master of Science.

Prof. Dr. Y. Ziya İder

I certify that I have read this thesis and that in my opinion it is fully adequate, in scope and in quality, as a thesis for the degree of Master of Science.

_____

Prof. Dr. Atilla Aydınlı

Approved for the Institute of Engineering and Sciences:

_____

Prof. Dr. Mehmet Baray

Director of Institute of Engineering and Sciences

# ABSTRACT

## IMITATION OF RADIOFREQUENCY ABLATION WITH FIBER DELIVERED LASER SYSTEM FOR MAGNETIC RESONANCE GUIDED TREATMENT OF ATRIAL FIBRILLATION

M. Can Kerse

M.S. in Electrical and Electronics Engineering

Supervisors: Prof. Dr. Ergin Atalar,

Asst. Prof. Dr. F. Ömer İlday

January, 2010

Atrial Fibrillation (AF) is among the most common cardiac arrhythmias with a high risk of mortality and morbidity. As a cure several minimally invasive catheter approaches are performed under imaging guidance. These treatments imitate linear and transmural cuts and sutures along the atrial walls similar to the widely accepted surgical Cox Maze procedure to block undesired currents. Catheter delivery of RF energy to the cardiac chamber is widely used and approved as safe and successful. The operation is commonly performed under X-Ray which is deprived of soft tissue contrast. Besides, combination of the image with ECG (electrocardiogram) data makes the operation technically difficult and time consuming. Due to the long exposure times, X-Ray burns may be seen on the patient.

MR images can be taken during RF ablation with proper matching and tuning circuits, however, during the operation RF and ECG catheters may cause artifacts in the image for some orientations. On the other hand, fiber delivery of laser energy has no significant MR compatibility issues and can be used under MR guidance. Nevertheless, MR guided laser ablation is not in clinical practice as a minimally invasive technique for curing AF possibly because of the risk of perforating the myocardial wall. Excess light intensity at the end of the fiber tip causes rapid changes in the temperature gradients which may cause charring. This is an undesired effect and especially in cardiac ablations, light intensity should be diffused. There are several diffusing tip designs to emit light in cylindrical symmetry, but, due to their orientation with respect to the cardiac chamber, common RF delivery methods cannot be applied directly.

In this thesis, we propose a novel multiple fiber laser energy delivery with catheter approach and a system that imitates the scars created with RF probes under MR guidance. The system closely imitates the ablation pattern of RF delivery and therefore is expected to have quick adaptation by physicians. As a proof of principle, we used 3 fibers oriented in different directions and obtained real time MR thermometry maps of the ex-vivo and in-vitro ablation zones during laser delivery. In addition, various light diffusion methods are considered for single fiber power delivery. We believe the combination of these methods will be the solution for the MR compatible RF laser ablation system.

***Key words:*** RF ablation, Laser Ablation, Minimally Invasive Approaches to Cardiac Arrhythmias, MR Thermometry Guided Ablations, Image Guided Interventions, Obtaining Spherical Ablation Lesions, Interventional MRI.

# ÖZET

## MANYETİK REZONANS GÖRÜNTÜLEME YARDIMI İLE ATRİYAL FİBRİLASYON TEDAVİSİ İÇİN RADYOFREKANS ABLASYONUNUN FİBER İLETİMLİ LASER SİSTEMİ İLE TAKLİT EDİLMESİ

M. Can Kerse

Elektrik Elektronik Mühendisliği, Yüksek Lisans

Tez Yöneticileri: Prof. Dr. Ergin Atalar,

Yrd. Doç. Dr. F. Ömer İlday

Ocak, 2010

Atriyal fibrilasyon (AF) mortalite ve morbidite riski yüksek olan ve en sık görülen kardiyak aritmiler arasında yer almaktadır. Tedavi olarak, atrial duvar boyunca doğrusal ve derinlemesine kesikler ve dikişlerle istenmeyen doku içi elektriksel akımları engelleyen ve yaygın olarak kabul gören cerrahi "Cox Maze" prosedürünü taklit eden ve görüntüleme eşliğinde gerçekleştirilen birçok minimal girişimsel kateter yaklaşımı mevcuttur. Kalp odacıklarında yapılan RF operasyonları yaygın olarak kullanılmaktadır ve güvenli olarak addedilmektedir. Operasyon yaygın olarak yumuşak doku zıtlığından yoksun X-Işınları altında yapılmaktadır. Ayrıca, EKG (elektrokardiyografi) verileri ile bu yetersiz görüntülerin yorumlanması ve uygulanması teknik olarak zor ve zaman alıcıdır. Dolayısıyla, operasyon sırasında uzun süre radyasyona maruz kalan hasta üzerinde radyasyona bağlı yanıklar görülmektedir.

RF ablasyonu sırasında uygun eşleme ve ayar devreleri kullanılarak MR görüntüleri alınabilmektedir, ancak operasyon süresince, belli oryantasyonlar için RF ve EKG kateter ve doku görüntülerinde bozulmalar görülmektedir. Öte

yandan, fiber aracılığı ile lazer enerjisinin taşınmasının, bilinen hiçbir MR uyumluluk sorunu gözlenmemiştir ve bu yöntem MR yardımı ile kullanılabilir. Fakat bu yöntemde miyokard duvarını delme riski olduğundan, yöntem AF tedavisinde kullanılmaz. Fiber ucundaki çok yoğun ışık şiddetinden ötürü, normal bir fiberin dokunduğu yerde ani sıcaklık değişimleri olmaktadır ki bu da kömürleşme adı verilen ve özellikle kardiyak ablasyonlarda istenmeyen bir etki yaratmaktadır. Bu etki, yoğun ışığın saçılmasıyla (daha geniş alana yayılması ile) elenebilir. Silindirik simetride ışık yaymak için birkaç fiber kateter ucu tasarımı vardır, ancak, ablasyon sırasında kalp odasına göre konumları nedeniyle, var olan RF dağıtım yöntemlerini doğrudan uygulamak mümkün olmamaktadır.

Bu tez çalışmasında, MRG yardımlı kateter yöntemi ile fiber ışığını çoklu fiberlerle kalbe taşıyacak ve RF ablasyon yaralarını aynen taklit edecek olan yeni bir lazer sisteminin ön çalışmaları yapılmıştır. Sistem, RF yanıklarını taklit ettiği için ve radyolojide RF kateterleri sıkça kullanıldığı için, operatör doktorun bu yeni MR uyumlu sisteme kolayca alışması beklenmektedir. Üçlü lazer fiber sistemi, ex-vivo ve in vitro denekler üzerinde yanıklar oluşturmak için kullanılmıştır. Ablasyon sırasında, oluşan lezyonun zamana bağlı sıcaklık değişimi ve şekli, gerçek zamanlı MR - Termometri görüntüleri ile teyit edilmiştir. Bunlara ek olarak, tek fiber ile ışığı küresel simetride saçma çalışmaları yapılmıştır. İnanıyoruz ki, bu yöntemlerin birleşimi, MRG uyumlu RF lazer sistemleri için çözüm oluşturacaktır.

***Anahtar Sözcükler:*** RF Ablasyonu, Lazer Ablasyonu, Ritim Bozukluklarında Minimal Girişimsel Yöntemler, MR Termometri Yardımlı Ablasyonlar, Görüntü Yardımlı Girişimsel Ameliyatlar, Küresel Ablasyon Yaralarının Elde Edilmesi, Girişimsel MRG.

# ACKNOWLEDGEMENTS

I believe that I am among those whose luck has been turned just at the time of hesitation. Thanks to my supervisor Prof. Ergin Atalar, I am now here, at the interface for combining different fields for the sake of humanity. Here, I express my gratitude especially to him, without whom I could never be aware of what was going on inside biomedical engineering field, also for always encouraging me and believing in me. Besides him, I wish to explain my appreciation to Asst. Prof. F. Ömer İlday for opening the doors of his Ultrafast Optics Laboratory to me; for helping me in learning another subject related to my research; for his entertaining, academic and very helpful discussions and for motivating me. I have learnt a lot from him.

My special thanks go to Prof. Orhan Arıkan and Prof. Levent Onural. Thanks to them, I am now considering to be given a PhD. degree and wish to become such great lecturers as them. I wish to thank Prof. Orhan Aytür for his inventive suggestions and for sharing his precious and limited time with me. I wish also to express my admiration to Prof. Ömer Morgül. He is still a hard rock music lover and when I look at him, I always tell myself that, I should never quit making music as an amateur musician and advanced electric guitar player. Also, I wish to thank him for coming to my concerts.

Lastly, I want to thank my office and home mate Haydar Celik for his full sincere support and for not distinguishing me from his brothers. Also, Adil Fırat Yılmaz and Emrah İlbey for their great helps during my experiments.

This work is supported by TUBITAK fellowship (BIDEB) 2228 for M.Sc. studies.

*My dearest mom, Mualla and dad, İlhan. Without you, I would have already been a guitar player finishing his career after graduation. Thank you for supporting me, thank you for always telling me that: "Nothing is valuable than our health, just be calm". Thank you for buying me my first guitar, thank you for letting me to make scuba-diving, go skiing and believing that these will always help me also in my career. Thank you music, all the great composers; Mozart, Beethoven, Haydn, Eric Johnson, Steve Vai, Marty Friedman and millions of others. Thank you my guitars, you have never left me alone while I was exhausted of making research. The most importantly, thank you Bahar Özkan, for joining me in my life just at the right time and painting it with the colors no one has ever seen.*

*……To those with cardiac arrhythmias*

# Table of Contents:

# List of Figures:

tissue. (b) Fiber is rotated by 45 degrees on the rz plane. (c) Fiber is rotated -45 degrees on the rz plane. (d) Sum of a,b and c.

Note: Intensities of the pixels are not considered since the desired absorption distribution has priority.

**Figure 5.1.2:** Three dimensional contour plot of absorption with single fiber excitation. The orientation of the fiber is shown with grey cylinder.

**Figure 5.1.3:** Three dimensional contour plot of absorption with the design given in Chapter 2. The orientation of the fibers and the excitation plane are shown with grey cylinders and white plate.

**Figure 5.1.4:** Three dimensional contour plot of absorption with inclined single fiber excitation. The orientation of the fiber is shown with grey cylinder.

**Figure 5.1.5:** Three dimensional contour plot of absorption with the design given in Chapter 2. The orientation of the fibers and the excitation plane are shown with grey cylinders and white plate. (Top View)

**Figure 5.1.6:** Three dimensional contour plot of absorption with the design given in Chapter 2. The orientation of the fibers and the excitation plane are shown with grey cylinders and white plate. (Side View)

**Figure 5.2.1:** Temperature graphs showing the rise of temperature of the gel phantom around RF electrode. (a) Temperature sensor is 2 mm away from the electrode through the surface and at the same level with the electrode through the depth. Delivered power is 0.7W (b) Temperature sensor is attached to the electrode and they are at the same level through the depth. Delivered power is 0.7W (c) Temperature sensor is attached to the electrode and they are at the same level through the depth. Delivered power is 1W

**Figure 5.2.2:** The lesion formed after 17.5W 1 minutes of RF delivery. (Left) Transversal slice. (Right) Longitudinal slice.

## List of Tables:

# CHAPTER 1

# INTRODUCTION

## 1.1 BACKGROUND

Atrial Fibrillation (AF) is one of the most common cardiac arrhythmias [1]. The atria (upper chambers of the heart) of a patient with AF fibrillates (quivers chaotically) rather than beating in its normal rhythm. These fibrillations occur due to the chaotic electrical activities in the atria. Usually, in a normal beating heart, the electrical activities originate from two contraction centers. The electrical signal first triggers the SA node to contract. This signal then travels along the electrically active cells to the AV node and through the hiss bundle; it branches and forms the normal beating rhythm [2]. However, in atrial fibrillation, there are several activation centers rather than the SA node, causing disoriented contractions. This kind of the behavior of the electrical activity makes the atria less effective and prevents blood to be less circulated. This inefficiency increases the risk of blood clots formation that could ended up with stroke.

The statistics show that AF is the most common arrhythmic cause for hospitalization and increases the stroke risk by 2 folds and mortality risk by 5 folds[3]. AF is responsible for about 20% of all strokes. By age 40, the remaining lifetime risks for atrial fibrillation are 26% for men and 23% for women. For patients age 85 and older, the rates of occurrences of atrial fibrillation are 1,077 / 100 000 in men and 1,204 / 100 000 in women [4].

There exist various pharmacologic treatments, however they frequently fail and are not enough for a complete cure [5]. In cases where drug therapy does not work a surgical operation called Cox Maze procedure is applied [6]. The operation is performed with multiple linear and transmural cuts and sutures within the atrial walls to block the undesired currents originating from those activation centers. The operation has some risks due to the open scars and bypassing of the heart; besides, it is lengthy and challenging [7]. Therefore, many researchers are investigating minimally invasive techniques such as radiofrequency ablation [8], focused ultrasound ablation [9], laser ablation [10], microwave ablation and cryoablation (cold therapy) [11]. The proposed method is not different than that is in the Cox Maze procedure. The aim of this catheter and focused energy approach is to imitate the incisions made with Cox Maze procedure with minimally invasive approach. Therefore, they are all based upon forming linear and transmural conduction blocks and the ones with catheter approach are called “catheter maze procedure” because of this reason [1].

### 1.1.1 THE COX MAZE PROCEDURE

The origins of the procedure were claimed by Cox et al. in 1980 [12]. Later in 1987, the Maze procedure was introduced as a curative surgical approach to atrial fibrillation [1]. Subsequently, the same group introduced Maze II and Maze III operations with some modifications [5]. After preoperative endocardial catheter electrophysiology studies are performed, the Maze procedure is applied by the surgeon. During this operation, the heart is bypassed and the blood flow is directed through the heart-lung machine. The heart is cut and sewed (this is also called “cut and sew” technique) to form multiple full thickness incisions. These incisions cause the currents originated from accessory pathways to be blocked.

Statistics show that the Maze procedure has 98% of success rate. In the long term, this ratio decreases to 95% [12]. Because of this high success rate,

the Maze procedure is widely accepted and applied also in catheter based treatments. However, technical complexity makes the procedure time consuming (on average 250 min). Also, complications due to postoperative bleeding may occur (with an incidence ratio 7% - 8%) [6, 7]. Therefore, research is being done to find alternative approaches to perform Maze procedure with minimal invasion.

### 1.1.2 RADIO FREQUENCY (RF) ABLATION

RF ablation can be considered as a new but promising technique in surgical operations. According to the statistics, number of articles published on RF ablation has increased from 19 to 828 between 1990 and 2005. Radiofrequency ablation has been utilized in a variety of areas [13], including tumor ablations [14] and cardiac arrhythmias [8].

Catheter delivery of RF energy to create linear scars in myocardium is a less invasive technique compared to surgical Cox Maze procedure as the cure of atrial fibrillation. Statistically, the survival rate amongst patients with AF underwent radiofrequency ablation is 97%, where, the rate of success of the operations is given as 76% in average. Moreover, the open surgery related postoperative symptoms are minimized with RF ablation. Therefore, catheter delivery of RF energy to the cardiac tissue in the cure of AF is widely used and considered safe and successful [6].

The principal of the operation is to apply high frequency current (100 kHz – 1MHz) at 20 – 150 W [7, 8, 11, 13] to the myocardial tissue through electrode catheters. There exist at least two electrodes to complete the electrical circuit. The smaller electrode is placed onto the myocardial wall and the larger one is used for grounding. Owing to the type of the RF ablation device

(unipolar, bipolar) the placement and dimensions of the grounding electrode may differ. RF energy is delivered to the distal tip electrode of the catheter. In the vicinity of the small electrode tip, the delivered energy needs to be dissipated through a small area with a high current density. Inside the frequency range of application, the tissue is mostly resistive [15, 16]. The high current density encountering high impedance cause intense heating in the vicinity of the contact electrode [8]. However, this resistive heating occurs within 1mm range. Therefore, rest of the ablation is due to the thermal conduction from the area where resistive heating occurs. Especially for unipolar catheters, the required ablation time is in the order of minutes. Even though it is the slowest method, it gives better control on the process [11].

There is a strict and vital relation between the electrical conductivity and heat generation. When tissue is heated, its conductivity changes with respect to the excess heating. Above $50^{o}$C, irreversible cellular destruction starts to occur and the regions in that range are considered as lesions [7, 17]. Generally, temperature controlled and irrigated tip RF catheters are used to increase the efficiency of ablation. The temperature control threshold value is adjusted to $70^{o}$C – $90^{o}$C [1, 18]. Because, at $100^{o}$C carbonization or char is formed at the electrode tissue contact area, which results in a sudden increase of electrical impedance [7, 13, 19]. The increase in impedance limits the current flow and increases the stroke risk while decreasing the chance of the creation of optimal lesion.

In order to increase the efficacy of RF ablation, studies are being made on thermal electrical modeling of the ablation process [8, 13, 15, 20, 21] and on temperature distributions in cardiac wall [22] with or without blood flow calculations. The blood flow calculations have essential importance for exactly representing the beating heart. At zero flow, lesion size will be largest but

charring may occur. The flow calculations are added after calculating the current density – heat related equations. The simplest relation between the current density and the heat is given as [8]

$$J = \sqrt{\sigma \rho SAR}$$

where J is the scalar current density ($A/m^2$), ρ is the density ($kg/m^3$), σ is electrical conductivity (S/m) and SAR is the specific absorption rate (W /kg). In their studies on 3D FEM (Finite Element Model) of RF ablation with blood flow, Jain and Wolf solve the simple Laplace equation of voltage distribution. There on, they develop their model by solving mass, momentum and energy equations.

$$\nabla \cdot \sigma \nabla \phi = 0$$

where Φ is the voltage distribution in the model. Then, with a quasi-static approach (by neglecting the displacement currents), distributed heat source $q$ is related as

$$q = \bar{J} \cdot \bar{E} = \sigma \cdot (\nabla \phi)^2$$

where, $E$ is the electric field intensity. Combining this electrically and thermally coupled problem with mass momentum equations yields a partial and complex differential equation called Penne's Bio-heat equation.

In their numerical model, Labonte *et. al.* [23] included the variations in tissue properties with respect to time for endocardial ablations. Since the temperature during the ablation is torrid, they ignore metabolic heat generation $Q_m$ and myocardial perfusion $Q_p$ of general heat equation and get the simple formula relating the temperature of the lesions and volumetric heat due to the conduction. It should be noted that to solve the differential equations, boundary conditions should be separately included.

$$\rho c \frac{\partial T}{\partial t} = \nabla \cdot (k \nabla T) + Q_v$$

Solving for temperature distributions does not always yield better comprehension of lesion dimension. It has been shown that temperature isotherms may poorly correlate with lesion size [24]. For this reason, in parallel to the simulative and mathematical approach, both in vivo and in vitro experiments are being conducted to gain a better understanding between the parameters of ablation and to get actual tissue damage patterns.

After RF delivery to myocardial tissue, lesions appear wider than they are deep. By endocardial ablation, Thomas *et. al.* obtained 3.8 ± 0.7mm deep and 8.1 ± 1.6 mm wide lesions by feeding the electrode with a 150W RF generator with target temperature of 85$^{o}$C for 60 seconds of ablation [18]. Similarly, Nakagawa *et. al.* also obtained 4.7 ± 0.6 mm deep and 9.8 ± 0.8 mm wide lesions [25]. The average thickness of the human atrium is less than 5 mm. However, thickness may show some variations over the atrial chamber and may increase up to 6mm [18]. As it is seen from both works, lesions are wider than they are deep. According to the statistics and research, larger lesions may improve procedure efficacy with a drawback of excess loss of atrial tissue which may reduce atrial contractility [1]. So, to obtain optimal lesion size and formation, the duration, delivery type (continuous or intermittent), applied power, electrode size and its orientation with respect to the atrial wall [25] should be properly adjusted.

### 1.1.3 LASER ABLATION

Laser (Light Amplification by Stimulated Emission of Radiation) energy delivery had been introduced to the medical field in late 1950s and emerged especially in ophthalmology field. Since then, it has been utilized in various

areas including tumor ablations, prostate treatment, certain cardiac arrhythmias and became a widely used procedure [26]. There are more than 20 laser types in the medical field to be used in several branches of the medical field. For example, Nd:YAG (Neodymium doped Yttrium Aluminium Garnet) at 1064 nm and 532 nm with second harmonic generation are among the most commonly used in many areas of medical fields such as ophthalmology and dentistry. Xe – Cl mid-infrared lasers have 2940 nm wavelength and used primarily on skin surgery. $CO_2$ lasersat 10 μm are used in dentistry and other areas. Diode lasers designed to operate at various different wavelengths are increasingly commonly used.

The main and discriminating attribute of a laser system is its wavelength. Tissue and materials have wavelength dependent absorption, which determines how deep a laser beam can penetrate into the material. Equally important is the type of energy delivery; continuous or pulsed, where pulse duration ($10^{-15}$ to $10^{3}$ seconds) together with the power density ($W/cm^2$) directly affects the type of interactions occurring inside the tissue. The physical mechanism of these interactions are greatly including, photochemical, thermal, plasma induced, photoablation, and multi-photon absorption. In addition to the properties above, with the invention of Q – switching, shorter pulse durations were obtained, where only pulse durations shorter than 1000 ns (the average relaxation time of excited tissue) provide non-thermal ablation. This process is primarily used not to cause any deformations in neighboring regions of ablation zone or to reduce the thermal side effects.

After the invention of fibers, the laser energy can be carried to further distances (or interventionally through the veins) without losing energy of incident light. In contrast to RF delivery, lasers rapidly create lesions. However, unlike RF electrodes, the light emitted from the fiber tip does not behave like a

point source. The beam is collimated, coherent, at a single wavelength and has a low divergence. In laser tissue interactions, fiber diameter, beam profile, spot size, irradiance and absorption are important parameters for ablation. Also, as explained earlier, optical properties of the tissue at operative wavelength are also decisive. At the fiber tissue interface, only the 3% of the light is reflected, while the rest of it penetrates into the tissue, where absorption and scattering take place. Turbid materials such as tissue are mostly absorptive [26-28]. In other words, absorption is the determinant effect relative to the scattering ability. Generally speaking, absorbance is the ratio of absorbed intensity over incident intensity. In visible spectrum, this phenomenon is related with the formation of colors. General absorption means color gray and selective absorption means the existence of a color. The absorption coefficient $\alpha$ ($cm^{-1}$) is highly correlated with penetration depth. Penetration depth is the depth where intensity of the collimated laser beam has been attenuated by a factor of $e^{-1}$. Since the absorption coefficient is highly depended on wavelength of operation, so does penetration depth. Technically speaking, absorption length $L = 1/\alpha$ measures the distance or depth z in which the distance dependent irradiance, or intensity I(z) has diminished to 1/e of its incident value $I_0$ ($I(z = 0)$, surface intensity). As an example, water absorption for 1060 nm near infra-red Nd-YAG lasers is $\approx 1cm^{-1}$. Then, absorption length L becomes $1/1cm^{-1} = 1cm$, which means at that wavelength, light travels through water for about approximately 1cm before its magnitude is decreased by 67%. Blue light ($\approx$ 460 nm) concedes poor penetration. On the other hand, near IR (infra-red) wavelengths (630nm – 1100nm) penetrates considerably deeper. This deeper penetration of light continues until the water absorption becomes dominant. $CO_2$ lasers having approximately 10,000 nm (1μm) wavelength shows almost no penetration. The tissue (which mainly composed of tissue and hemoglobin) shows almost highest absorption at that wavelength, so that the light is absorbed rapidly at the surface. This process is mainly used on surface excitations and skin surgery.

Ablation of a tissue is a thermal process and it is obvious that a thermal process is related with absorption. After a region absorbs incident light energy, it gets heated. This is similar to RF heating consequent to resistivity related power dissipation. Then, the heat is transferred by conduction and diffusion. For example, heat diffuses in water approximately 0.7μm within 1μs, thus for thermal processes, it is important to adjust the duration [26]. According to Welch, heat deposition due to absorption is based on exponential attenuation. His claim is that this attenuation is not only affected by absorption and also it is due to scattering in all directions. To understand the whole effect, light propagation can be solved with mathematical theory based upon Maxwell's equations [27, 29]. Although this approach includes all diffraction effects, it is mathematically complex. The approximate solutions to this problem are originated from light diffusion theory [26-29]. In [28], Welch assumed light is predominantly forward scattered near the surface (within 1mm). As a result, beyond that depth, the light distribution becomes isotropic, in other words, diffuse radiance has a wide angular spread. The basic absorption and heat relation is given in Figure -1.1[28].

Heat is closely related with irradiance I(r, z) or intensity at the distance z,

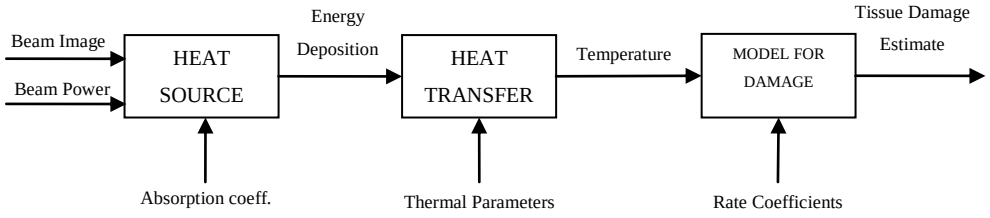


Figure 1.1 Block diagram of the thermal events in laser irradiated tissue

where

$$I(0,z) = I_0 e^{-\gamma z}$$

Here, $I_0$ is *I(z = 0)*, in other words, intensity of the incident light. $\gamma = \alpha + \beta$, where $\gamma$ is called as attenuation coefficient (1/cm), $\alpha$ is absorption coefficient

(1/cm) and β is scattering coefficient (1/cm). including the effect of the radius r, the heat deposition Q(r, z) is defined as

$$Q(r,z) = \frac{\partial I(r,z)}{\partial z}$$

where

$$\frac{\partial I(r,z)}{\partial z} = \alpha I(r,z) + \beta I(r,z)$$

where the second term on the right hand side does not contribute to heating for this simple illumination case. Then,

$$Q(r,z) = \alpha I(r,z)$$

which is a linear relation. However, for detailed simulations and calculations, it should be noted that scattering and reflection effects also contribute to heating and α can be a function of r and z, α(r, z). Similar results had been achieved also by Kubelka – Munk and became a theory [26]. What this theory says about the relationship between heat and irradiance is similar to the above formulations. They approximated the intensity (irradiance) as

$$I(r,z) \approx e^{-z\sqrt{[A+(A+2S)]}}$$

here, A is the absorption coefficient and S is the scattering coefficient. With their assumptions, the heat deposition becomes

$$Q(r,z) = AI(r,z)$$

which is the same as the equation given by Welch. In their work Motamedi *et. al* [30] summarized this relation and obtained a more detailed equation at the end. The procedure they followed is summed up as below.

$$I(r,z) = I_0 e^{\frac{-r^2}{2\sigma^2(z)}} e^{-(\alpha+\beta)z}$$

where, $\sigma^2(z)$ is the standard deviation of the laser beam within the tissue. In the case of no absorption ($\alpha = 0$) the beam would broaden and the power at any random depth would be equal to the power at the surface (incident beam).

$$P(z) = 2\pi I_0 \sigma^2(z) e^{-z\beta}$$

and

$$P(0) = 2\pi I_0 \sigma^2(0)$$

where

$$\sigma^2(z) = \sigma^2(0) e^{z\beta}$$

in a similar manner

$$Q(r,z) = \alpha I_0 e^{\frac{-r^2}{2\sigma^2(0)\exp(\beta z)}} e^{-(\alpha+\beta)z}$$

and their proposal is, if the absorption takes place only in the direction of incidence, $Q(r, z) = \alpha I(r, z)$ which is the same as the equation of Welch *et. al.*

The general temperature change is given as

$$\frac{\partial T}{\partial t} = \frac{k}{\rho c}\left\{\frac{\partial}{\partial r}\frac{1}{r}\frac{\partial T}{\partial r} + \frac{\partial^2 T}{\partial t^2}\right\} + \frac{Q}{\rho c}$$

where T is the temperature, k is the thermal conductivity, c is the specific heat constant and ρ is the density.

Temperature at a highly absorptive lesion rapidly increases and gets carbonized, which may be an undesired effect during most of the operations, especially in the treatment of AF. At a carbonized interface, the tissue becomes more and more absorptive and prevents the incoming light from penetrating deeper. This excess water loss inside the tissue causes sudden drop in heat conductivity and heat diffusivity and encountered mostly in CW (continuous wave) ablations, which prevents the transfer of heat.

Laser energy has deeper penetration ability. However, for catheter ablation procedures, the light energy should be directed with the help of fibers. The light intensity at the tip of a fiber is high. This excess intensity is also limited to the diameter of the fiber core. Whenever such a system makes contact with tissue, due to the higher temperature gradients, char may be formed and optical tissue properties may change rapidly. Especially in the field of cardiac ablations, as explained previously, char formation is an undesired effect and is tried to be reduced with the help of irrigated tips. Novel approaches are in the direction of fabricating diffusing tips so that the intense light exiting from the fiber is diffused homogeneously and confined into a larger volume.

Detailed heat simulations by using Method of Finite Differences or by any other method was done for heating corresponding to light diffusion. However, the simple equations above are sufficient to understand the analogy between RF heating and absorption related heating.

## 1.2 MOTIVATION

Catheter delivery of RF energy to the cardiac chamber is widely used and approved as safe and successful [7]. The operation is commonly performed under x-ray, which suffers from poor soft tissue contrast. In addition, the surgeon has to decide whether the local ablation is successful by looking at the simultaneous ECG data, which makes the operation technically difficult and time consuming. Due to the long exposure times, x ray burns may occur.

MR imaging during RF ablation is possible with proper matching and tuning circuits [31-33]. However, during the operation RF and ECG catheters may cause artifacts in the image for some orientations. On the other hand, fiber delivery of laser energy has no MR compatibility issues and is used with MR

guidance in the field. It is not widely used in treatment of AF, since there is a risk of perforating the myocardial wall. Several diffusing tip designs have been proposed to emit light in cylindrical symmetry [34-38] to produce a more even effect, but, due to their orientation with respect to the cardiac chamber, common RF delivery methods cannot be applied and imitated directly. These, designs diffuse light in cylindrical geometry. Besides, due to their design specifications, they cannot be directly used in place of RF probes in the treatment of AF. However, for tumor ablations, they may be quite useful.

Except from the image guiding hardware issues, the aspects of ablation lesions and side effects of RF delivery and laser ablation is a contemporary issue [11, 13, 15]. Charring may be formed by both of the techniques. To prevent this, irrigated catheter tips are designed and applied with proper combination of delivery types; intermittent delivery for RF and pulsed delivery for laser ablation. However, the quarters wherein the myocardial wall thickness has increased may not be ablated transmurally, where, shallower regions are, during RF delivery. Due to this improper situation, the chaotic atrial rhythm may recur. On the other hand, light may penetrate deeper into the cardiac wall and the transmurality may be obtained. Yet, for shallower zones, there still remains the risk of perforating the myocardium.

The lesions (scars) formed after ablation can be compared with respect to the lesion depth, width or a depth to width ratio can be defined as a comparison criterion [10, 39]. With novel MRI sequences, post ablation RF scars can be visualized [40]. Besides, MR thermometry is newly developed tool to visualize the temperature maps of the ablation zone for laser interventions [41].

## 1.3 SUMMARY

Here, we propose a novel multiple-fiber scheme for delivery of laser beam that imitates the scars similar to those created with RF probes under MR guidance. This scheme imitates the ablation pattern of RF delivery and as such is expected to have quick adaptation by physicians. The finished ablation system will consist of several pumped diode lasers which are cheaper and much smaller in size as opposed to the current bigger medical laser systems. Besides imitating the RF scars inside the tissue, the laser probe handle will also resemble commercial RF probes and it is going to be tractable under MR. Moreover, with the guidance of MRI and MR thermometry, surgeon will be able to visualize the lesion of ablation and its temperature and decide the success of a zone by combining the temperature maps with real-time ECG data.

As a preliminary demonstration, we used a 3-fiber scheme supported by real-time MR thermometry maps of the ex-vivo and in-vitro ablation zones during laser delivery. Moreover, some other designs, which are more suitable for insertion into the blood vessels, are also experienced, and the lesions are compared. Lesions and/or melts (for gel phantoms) created with RF and laser delivery are also compared with respect to their width, depth and depth to width ratios.

# CHAPTER 2

## THEORY

Main principles of creating ablation lesions by both RF and laser energy delivery methods are similar. The high current density at the tip of the RF probe encounters high impedance and causes heating. This resistive heating is then transferred to the neighboring tissue through heat conduction. The unipolar electrode tip creates half-spherical lesions. In case of laser ablation method, absorption is the main mechanism of energy transfer. Locally absorbed energy is transferred to a larger volume by the heat conduction mechanism. Typically the depth of a RF induced lesion is less than its width but the laser induced lesions are deep but not wide. This fact may be the main reason why the physicians prefer RF ablation over laser ablation in the treatment of AF.

RF ablation lesions can be imitated with laser fibers, if the SAR (Specific Absorption Rate) distribution due to the electrode tissue interaction can be copied exactly. It can be thought such that the lesions are related with the temperature of the tissue, where SAR is related with the power capacity of the tissue per unit mass.

As it is mentioned in Chapter 1, absorption coefficient, which determines the penetration depth, is related with the wavelength. So, appropriate choice of wavelength is crucial. Besides, the orientation of a fiber with respect to the tissue may change the shape of the lesion. Thus, any desired lesion can be created by modifying the wavelength and the orientation, where, this approach will give two degrees of freedom in the design of tip orientation. However, only one fiber (two parameters to change) will obviously be in case of forming wider

lesions. Inefficiency of single fiber may be compensated by using a multiple fiber scheme to obtain RF – like half spherical lesions. This gives us 2*N degrees of freedom (N is the number of fibers). Moreover, diffusing or refracting tips may be designed to be inserted at the tip of a bare fiber to get the same effect.

The wavelength of the laser should be chosen properly so that the light will be able to penetrate more to compensate RF ablation defects in obtaining perfect transmural lesions within the tissue. In other words, we should be interested in the wavelength interval wherein the absorption coefficient has minimum. Wavelength dependent coefficients for many organs and species are available in the literature [42]. Also, the available data are generally for commercial medical lasers at distinct wavelengths. For example, at 1064 nm wavelength, human myocardium has $\mu_a = 0.3$ $cm^{-1}$. Also, in the region of 600 – 1300 nm range, tissue absorption is lowest and has small fluctuations [42-47]. In the light of the available data related to the optical tissue spectra and considering the availability of lasers, wavelength of operation should be chosen in the vicinity of 1000 nm. At this wavelength range, there are cheap pumped-diode lasers (980 nm) are available to be used for simple, portable and easy-to-implement setup. A detailed absorption coefficient vs. wavelength graph is given in Appendix B.

First of all, the effect of a single fiber should be investigated. Computer simulations including photon transport theory can be done for single and multi-fiber excitations. Besides, instead of using multi fibers, refractive tips can be designed to diffract the incoming light so as to have a point source at the interface. This design method could then be used for interventional procedures since the will be narrower than the diameter of the blood vessels.

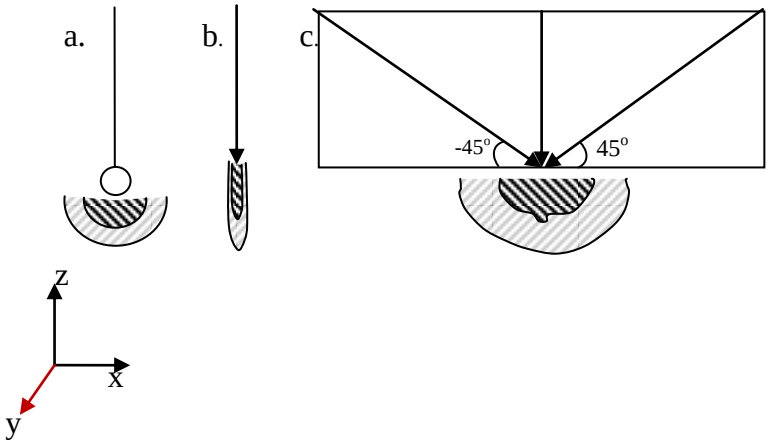


Figure 2.1 – Schematic description of lesions obtained with different transducers. a. Unipolar RF electrode lesion b. Single fiber excited lesion c. Our three fiber design and expected lesion

The beam exiting from a single fiber has a Gaussian shape, creating narrow and deep lesions (Figure 2.1 b). It is assumed that the tissue characteristics are both temporally and spatially linear (negligible variations in absorption, scattering coefficients during the initial period of ablation). Virtually any desired lesion pattern can be obtained by changing the number of fibers, their orientations and wavelengths. A simple approach is to place three fibers in the orientation shown in Figure 2.2, where the impulsive absorption (J/cm3) responses spatially add up and create a half circular lesion in the xz plane, Figure 2.1 c. The rest of the energy will then be dissipated deeper into the tissue in a circular geometry. With this approach, only 2D slice in one plane (let say xz) of the RF ablation lesion can be imitated. However, for 3D half spherical lesion imitation, more fibers are needed lying in other planes. Yet, if half circular 2D lesion can be obtained, it can be concluded that it is possible to get 3D half spherical lesions. In addition to the multi fiber scheme in Figure 2.1c, spherical ended capillary glass tubes may be used to obtain the 3D effect. The air glass interface will refract the light exiting the fiber (de-focus), and spherical patterns can be obtained. Since we want to spread light as much as possible, numerical aperture (NA) of a fiber can be another parameter to play with. Numerical aperture is a dimensionless measure of angular span of the light exiting from a fiber. The higher the numerical aperture is, at wider angles the

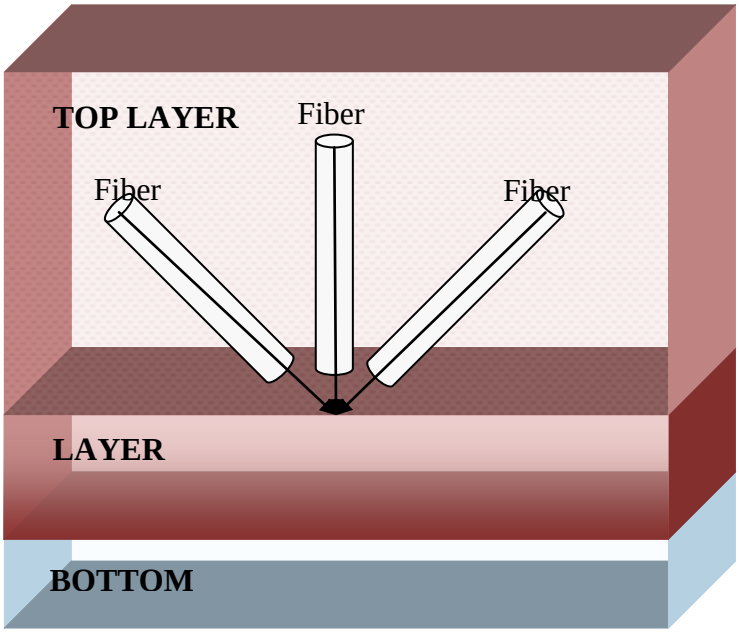


Figure 2.2– The proposed fiber orientation to imitate RF scars. The LAYER phenomenon is used for light diffusion simulations (MCML code) of Wang et. al. 1995. TOP LAYER is blood. LAYER is endocardium and BOTTOM is air (body cavity).

fiber can emit light. So as to have more angular spread, it is better to use high numerical apertured (NA) fibers (0.22 or 0.40). Also, with the help of high NA, the accumulation of focused light energy at a single point can be averted.

To understand the wavelength, power and fiber orientation related effects, either photon diffusion equations can be solved or photon transport simulations can be done. Mathematical descriptions and formulations for propagation (absorption coefficient related) and scattering characteristics of light can be done via Maxwell's equations and transport theory. Instead of solving mathematically complex wave equations, simulations are carried out via photon transport theory, which is used in a large number of applications [27].

The real-time orientation dependent light penetration effect may be visualized inside a gel phantom by noting the deformations inside (melted regions) or by taking slices of the ablated lesions of the tissues. By applying high intensity current to the laser in a short period of time (short enough to ignore the heating effects), the lesions formed prior to the excess heating can then be assumed as absorption distribution (SAR). However, it is hard to implement such an impulsive system and visualize its effects. Besides, there is no experimental validation of SAR results for RF ablation to compare with. So, temperature distributions of the ablated zones for both RF and laser deliveries can be compared. Usual RF lesions are almost half spherical but wider than they are deep with width $8.1 \pm 1.6$mm and depth $3.8 \pm 0.7$ mm (in endocardial left ventricle cardiac tissue of Merino Wether sheep) [18]. As it is explained in Chapter 1, absorption, heat and temperature are related to each other. By assuming a perfusionless medium, as it is in this case, we may assume that the shape of the temperature distribution can give an idea in visualizing the shape of the SAR pattern. Then, the lesions (or melted regions inside a gel phantom) can be compared by their width, length or depth to width ratios. The designs in Figures 2.1c and 2.2 will obviously create a vertical slice of a half sphere. However, with more fibers and/or some scattering media, the light could be directed to form half spherical (3D) ablation lesions.

# CHAPTER 3

# SIMULATIONS

To understand the SAR pattern of single laser beam perpendicularly exciting the tissue, Monte Carlo -modeling based photon transport simulations are done with the help of a C code written in 1995 by Wang *et.al.* [48]. The results for single fiber are then fed into a MATLAB subroutine to understand 2D and 3D effects for multi-fiber excitations. Only the SAR pattern shape is considered to have an insight about the temperature distribution of multi-fiber scheme (hand-fan design). No comparison with RF delivery is done in this chapter.

## 3.1 BACKGROUND

Simulating the behavior of the light in turbid medium has always been a challenge. Especially the laser tissue interactions simulations are all by itself a research area. There are optical simulators available in the market like LATIS, LATIS3D and ZEMAX. The most detailed computer program for modeling laser tissue interactions is LATIS where those interactions are divided into processes, thermal effects, material effects and hydrodynamics bases [49]. Actually, LATIS and LATIS3D are not yet commercial and are still under development and used at Lawrence Livermore National Laboratory. ZEMAX is a lens design and ray tracing program and on the basis, it does not contribute more to laser tissue interactions. Except for LATIS software, simulating laser tissue interactions for every tissue type is something that is still under development.

There is not much tissue data for all wavelengths. The laser tissue characteristics are measured, simulated or the statistics needed for tissue

characteristics are interpolated with the help of commercially available lasers just for a few varieties of mammalian tissues. Moreover, the important coefficients forming the basis of the laser tissue theory can be sometimes hard to measure and is also a research area. While using such software or solving optical wave equations, one needs to know those specific coefficients.

## 3.2 MONTE CARLO MODELING BASED APPROACH

For photon transport theory simulations, an open source ANSI C code (Monte Carlo Modeling of Light Transport in Multi-layered Tissues in Standard C) has been used [48]. The code uses Monte Carlo simulation essentials. Monte Carlo simulations are all based upon a stochastic model that is constructed in which the expected value of a certain random variable is equivalent to the value of a physical quantity to be determined. Here, a photon is not considered as a wave and phase and polarization effects are ignored. It is explained as the irradiative energy transport in turbid tissues [26].

As the first input to the program, one needs to define the characteristics of the medium of interest layer by layer. For every layer, the corresponding constants should be defined. The code is for an infinitely narrow photon beam perpendicularly incident on a multilayered tissue [48]. Because of this phenomenon, we cannot rotate or tilt the fiber position and adjust its width. However, as will be explained later, we may use it as both spatial and temporal impulse response. Since the approach is based on a stochastic model, the absorption coefficient $\mu_a$ and the scattering coefficient $\mu_s$ are defined as the probabilities of photons absorption and scattering per unit infinitesimal path length. Clearly, the output will give us a result about a photon's probability of reaching somewhere in r and z coordinates. Here, absorption A(x,y,z) (energy per unit volume) and fluence $\varphi$(x,y,z) (energy per unit area) outputs are considered and the data is then regulated with MATLAB with respect to z and r coordinates as the first step to understand how far a light is able to penetrate

before it is absorbed by the material (tissue) at the wavelength of simulation (1064 nm) ( $\mu_a \varphi(x,y,z) = A(x,y,z)$).

A simple input to the MCML (Monte Carlo Modeling of Light) should include scattering coefficient, absorption coefficient, refractive index and anisotropy factor at that specific wavelength for each layer (Figure 2.2). Also, the energy and the shape of the beam (Gaussian or flat) are important parameters to be defined. The coefficients for various wavelengths are taken from [42].

Mainly, five types of interactions occur when a laser beam is applied to the tissue. These are photochemical interactions, thermal interactions, photoablation, plasma-induced ablation and photodistruption [26]. The MCML does not consider any of these interactions. Also, after the tissue gets heated too much, carbonization occurs through the surface where the light applicator is in contact with. This induces rapid increase in tissue absorption characteristics and blocks the laser beam and avoids its penetration [26, 39, 50]. The MCML program does not consider this change in the behavior of the tissue with respect to time, also. The only output that is modified and used as an input to the MATLAB code is the fluence and absorption outputs. Here, we are not much interested in the simulations that is how deep the light reaches into the tissue; rather the first aim is to imitate the SAR pattern that an RF ablation probe creates on endocardium and inside the myocardium. It is also obvious that a photon packet has the probability of penetrating deeper into the layer, if the absorption coefficient gets smaller. So, MCML will only give this extended pattern. Moreover, as previously mentioned the stochastic process considers infinitesimally narrow photon beams that are incoming perpendicularly on our layer. The duration of the beam is also infinitesimally small. So, we have a system, which consists of an infinitesimally small laser beam exciting the layer (tissue) only in the perpendicular direction. We apply an impulse to that system

and get the SAR pattern for only single beam excitation. This single beam SAR response is then regulated to understand the effect of multi-fiber schemes in both 2D and 3D cases.

The fluence or absorption outputs of the MCML programs are one dimensional arrays. For our particular application, the outputs are 2 column vectors, one for axis **r** and one for axis **z**. This type of MCML output is first regulated (converting these 2 columns into an image) with our MATLAB subroutine and converted to a 2D array to be displayed and color-mapped with respect to intensity. A**s** mentioned in section 2.1, we assume the tissue linear (the tissue coefficients do not change with respect to time and position) and by rotating and adding each impulse response, we observed circular absorption response in 2D. The rotation processes are done by first cropping the desired region of interest and multiplying it with a rotation matrix in 2D. Another subroutine is written to calculate new coordinates of the rotated pixels to be used later in the overlapping process. Then, the subsequent rotated images are added to each other pixel by pixel and resulting image is considered as our new absorption or fluence output. Only two rotations are done along one axis to obtain (three fiber scheme) half circular SAR pattern in 2D. In other words, three fiber tips are assumed to be used. After we had an insight that we may have a circular absorption pattern with only three fibers, the fibers (2D absorption images) are rotated along their axis of penetration by $180^{o}$ to obtain 3D absorption patterns of each fiber. Here, the cylindrically symmetric feature of a fiber laser is taken into consideration. Then, after adjusting the centers of each 3D volumetric data to overlap each other, the 3D data are added voxel by voxel and the resulting 3D matrix is smoothened with MATLAB "smooth" function. We are only interested in shape of the absorption and/or fluence images, so smoothening helps us to visualize the regions of absorption more clearly. The overall process is described in Figure 3.2.1 and Figure 3.2.2.

In simulations, the SAR effect of single fiber orientation is observed at the wavelength of operation. Then, three-fiber scheme (hand-fan design) is simulated and it is seen that even in 2D simulations, half circular SAR pattern can be obtained with only three fibers lying in the same plane. Also, 3D simulations of the orientation given in Figure 2.2 shows that, half circular absorption pattern is obtained in the xz plane (refer to Figure 2.1), where, a narrower (in the width of single fiber excitation) pattern in zy plane. The absorption pattern created by the bubble ended capillary refractor tubes cannot be simulated with this available program, rather, they can be only experimented. The results belonging to the hand-fan design are given and discussed in Chapter 5.

The shape of SAR pattern is not our comparison criterion. However, it gives us an insight about what the temperature map will look like inside a perfusionless media. Moreover, novel multi-fiber designs can be simulated in this manner, before experiments are conducted.

For cardiac ablation simulations, the motion of the heart, the cooling effect of the blood over endocardial surface are also needed to be taken into consideration, which makes most of the work harder. However, in this part, we ignored those effects.

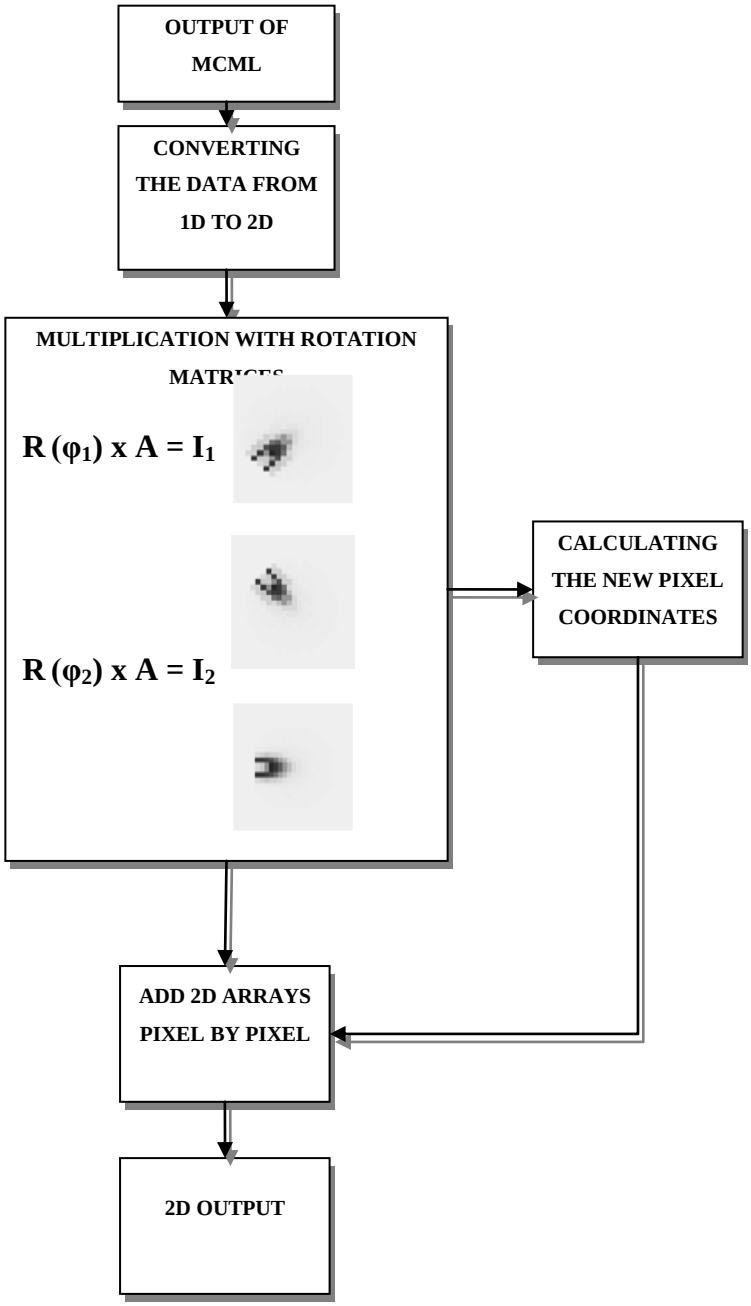


$R(\phi_i) = \begin{bmatrix} \cos\phi_i & -\sin\phi_i \\ \sin\phi_i & \cos\phi_i \end{bmatrix}$ where i = {1,2} and φ = {45°, -45°}.

A : Absorption Matrix

$I_1$ and $I_2$ : New rotated intensity matrices

Figure 3.2.1 – Flowchart of 2D rotate and add operation

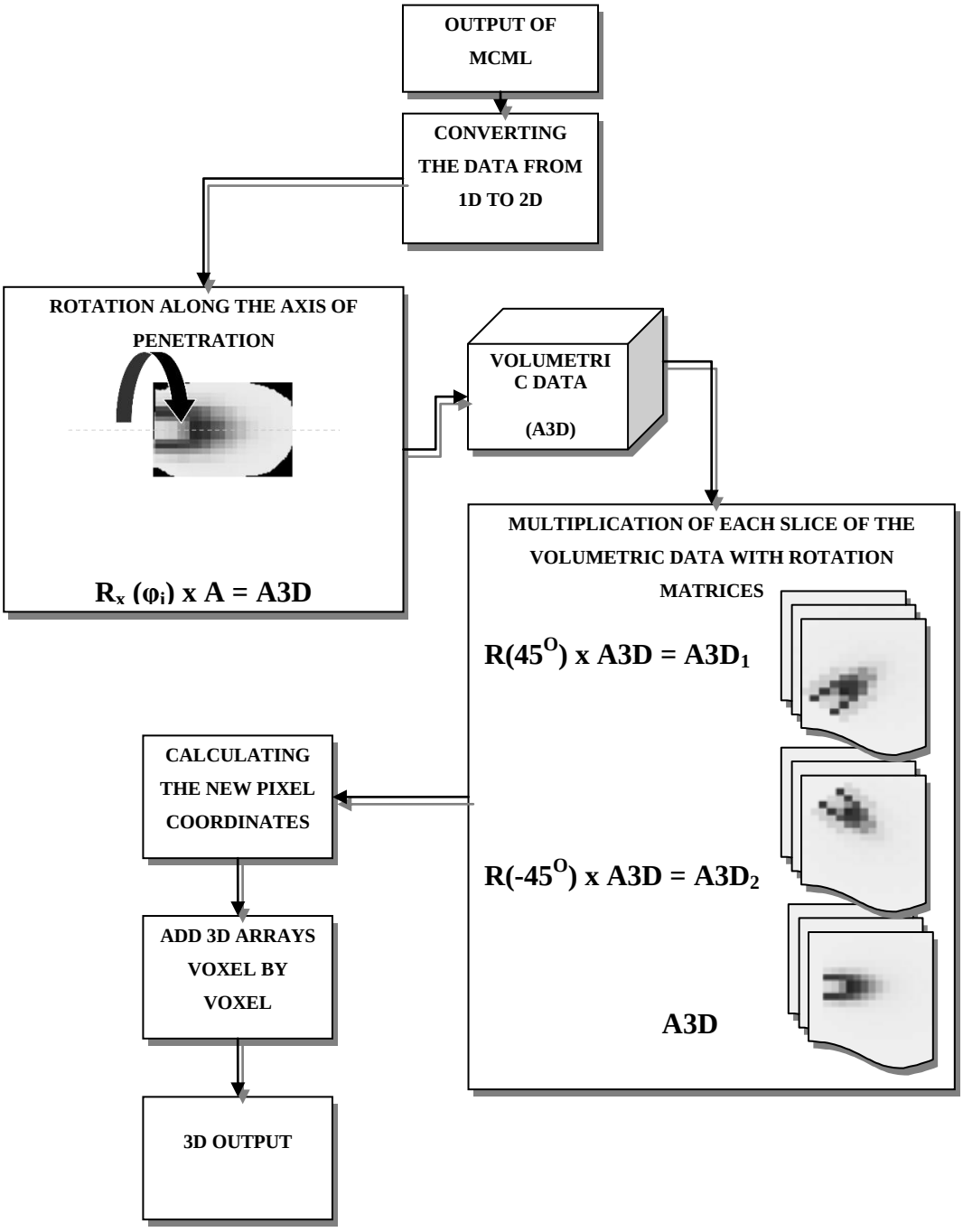


$$R_x(\phi_i) = \begin{bmatrix} 1 & 0 & 0 \\ 0 & \cos\phi_i & \sin\phi_i \\ 0 & -\sin\phi_i & \cos\phi_i \end{bmatrix} \text{ where } \varphi_i = \{1^o, 2^o, \ldots, 179^o\}$$

A3D : New 3D Volumetric Absorption Matrix

Figure 3.2.2 – Flowchart of 2D rotate and add operation

# CHAPTER 4

## EXPERIMENTS

In this section, the experimental methods to test the performance of proposed laser ablation systems are shown. In their experiments, Thomas et al. showed that multi-electrode RF catheters create lesions that are almost half spherical but wider than they are deep with width 8.1 ± 1.6mm and depth 3.8 ± 0.7 mm in endocardial left ventricle cardiac tissue of Merino Wether sheep [18]. The general aim of the experiments here are to match these lesion dimensions by using laser probes.

To compare the lesions formed by both our laser system designs and commercial RF probe, gel phantoms (prepared with Dr. Oetker banana gel) and tissue experiments (beef) are conducted. Even if the absorption is significantly less compared to tissue in this semi-transparent phantom, the shape of the ablated region can easily be observed via naked eye during the ablation processes for both laser and RF probes. Since the banana gel phantom consists mainly of water, the absorption coefficient is assumed to be in the vicinity of water absorption coefficient at 1000 nm (0.1 $cm^{-1}$). To include the cooling effect of blood, the gel phantom and the tissue are put in water. Blood flow may change the shape of the ablation region. When we use the RF in a phantom it creates heating in a half-spherical region. If we can imitate this profile on phantom with laser, this system will behave similar to RF ablation in in-vivo conditions.

Temperature distribution is related intimately with the absorbed energy, so, MR thermometry images and sections of ablated lesions on both phantoms and tissues can be compared with simulation results. It is known that average atrial thickness in normal human myocardium is 4mm [51]. So, MR monitoring

of thermal changes and/or soft tissue thickness could be more than a powerful tool to be used by the operator.

## 4.1 RF EXPERIMENTS

### 4.1.1 RF GEL EXPERIMENTS

To see how a unipolar RF ablation catheter forms melts in the gel phantom, the setup in Figure 4.1.1 is prepared. The power amplifier used is not an original one that is used in regular RF ablation processes. The commercial amplifiers usually work between 350 and 1000 KHz [6-8, 52] and can dissipate more than 50 W depending on the type of the process. A 100W audio amplifier rack is used (TKS100 – 100 W Relay Protection) in the experiments. It should be noted that the audio amplifiers operate in the linear region between 3 – 20 KHz. When this interval is exceeded, the amplifier start to operate in the non-linear region and the output signal intensity may drop. Yet, for our particular case, the amplifier is used at 90 KHz. When the input of the audio amplifier is fed with a sinusoidal signal at 90 KHz, the reduction in the output signal intensity (as it is compared to the value in the linear operating region) drops by 12%. After this value, the sinusoidal shape of the signal at the output is not maintained and signal intensity drops suddenly. Although 90 KHz is not in the operating frequency range of commercial RF ablation amplifiers, for the lesion size comparison purposes, it can be an acceptable value. Besides, for gel phantom experiments, 1W may already be an enough. So, the signal intensity drop at the output has not much importance, where our each laser diode (JDSU 10W pumped diodes) contributes maximum 10W power.

Signal generator is directly connected to one of the 4 line inputs of the amplifier. A stereo jack is used as a connector. The output of the amplifier has a DC resistance of 8 Ω, where our load has ≈ 250 – j3 Ω impedance, where the load impedance (RF probe -> gel phantom -> 10 Ω -> ground plate) is measured by a Network Analyzer (HP – 8753/D). It is seen that the imaginary part has a

capacitive effect arising from the high dielectric constant of the gel. Impedance of our system is then matched to the output resistance of the audio amplification rack with the circuit given in Figure 4.1.1 to be able to transfer maximum power to the electrode. After doing so, the amplifier is fed with sinusoidal input with 0.330 $V_{pp}$ at 90 kHz. Between 0 – 3 min of RF delivery to the gel, deformations (internal melting) were observed. The results are obtained for 0.7W 90 seconds, 0.7W 200 seconds and 1W 140 seconds deliveries. Only the temperatures of some locations are recorded to see whether heat convection takes place.

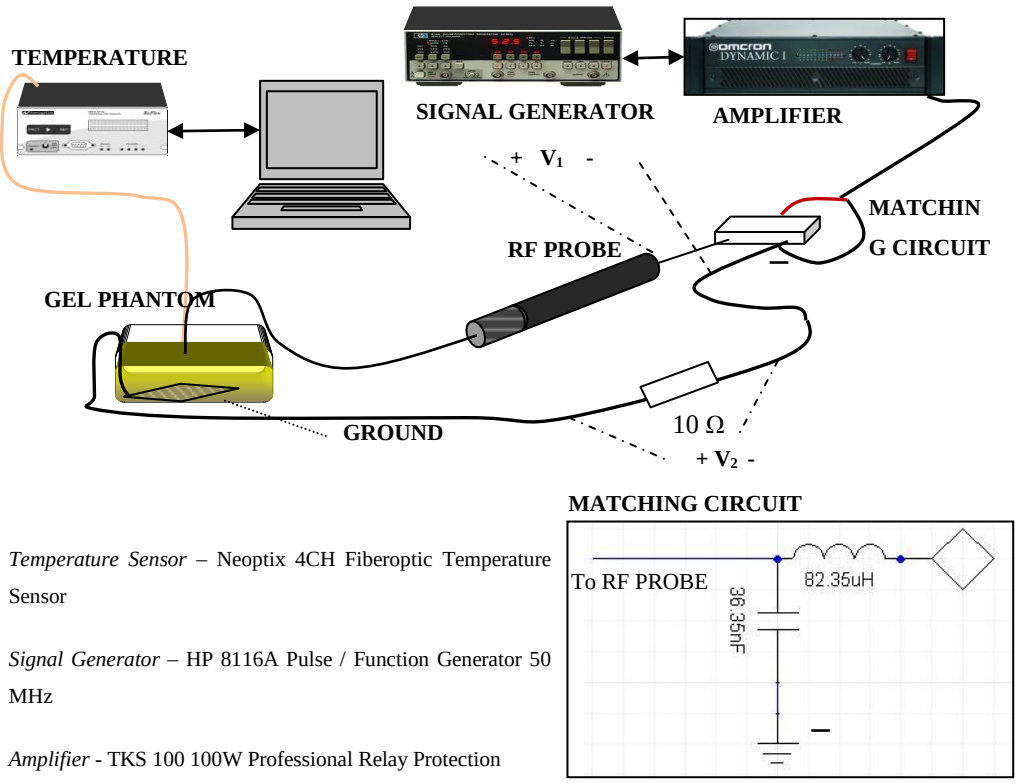


*Temperature Sensor* – Neoptix 4CH Fiberoptic Temperature Sensor

*Signal Generator* – HP 8116A Pulse / Function Generator 50 MHz

*Amplifier* - TKS 100 100W Professional Relay Protection

Figure 4.1.1- RF Ablation System

To measure the current passing through the system, a high power capacity (10W) 10 Ω resistor is connected is series, in case of flow of high output current through the wires.

Figure 4.1.2- Gel Phantom and electrode orientation

## 4.1.2 RF TISSUE EXPERIMENTS

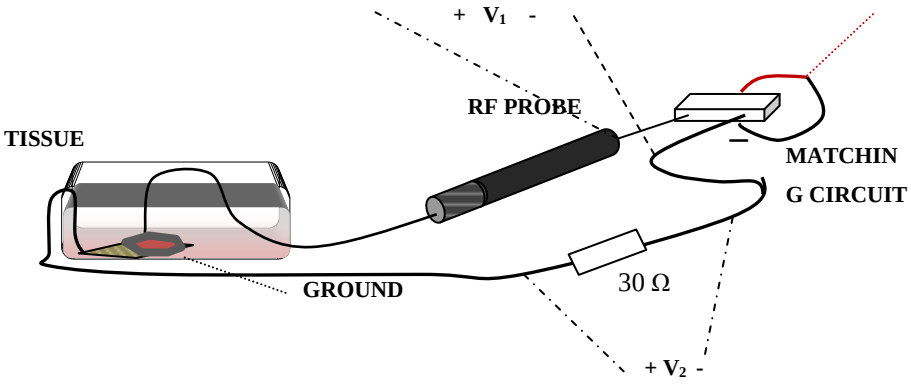


Figure 4.1.3- Modified part of the setup in Figure 4.1.1 for tissue experiments

To record the output power dissipated in the tissue, some modifications are done to the setup seen in Figure 4.1.1. First of all, the output impedance of the audio amplifier is found in the vicinity of 2.5Ω as opposed to the given output impedance value (8Ω) at the back of the system. This is done by terminating the output of the amplifier with 10Ω, 5Ω, 3.3Ω, 2.5Ω separately and measuring the voltage on the termination resistor. Maximum power is observed when the output is terminated with 2.5Ω. Since we need to deliver enough power to ablate the tissue (10 – 20 W), the matching circuitry was changed and new load is considered as RF probe, tissue, ground plate and the additional 20Ω which was connected in series to read the voltage on it. The new matching circuit consists of a shunt 62 μH and a series 94 nF from the load end. The modified part of the setup and the measurement terminals are shown in Figure 4.1.3. To measure the current passing through the system, three high power capacity (10W each) 30 Ω resistor is connected is series, in case of flow of high output current through the wires.

$V_1$ and $V_2$ are measured with the help of a 2CH oscilloscope. (Agilent Technologies InfiniiVision 350 MHz DSO7032A )

Since the input and the output waveforms are sinusoidal, the output power is calculated as :

$$P_{out} = I * V * \cos\theta = \frac{V_2}{30} * V_1 * \cos\theta$$

where θ is the phase difference between the voltage waveform and the current waveform. To ablate the tissue, the amplifier was used in its limits. $V_{1pp}$ = 78V , $V_{2pp}$ = 8V and θ = 30°. So the power delivered to the tissue is 18 W.

The inital temperature of the electrode tissue contact was 21°C The increase rate of temperature is given below:

| Time (seconds) | Temperature ($^{o}$C) |
|---|---|
| **20** | 50 |
| **30** | 58 |
| **60** | 62 |

Table 4.1.1 - The temperature rise with respect to time, for RF tissue ablation experiment

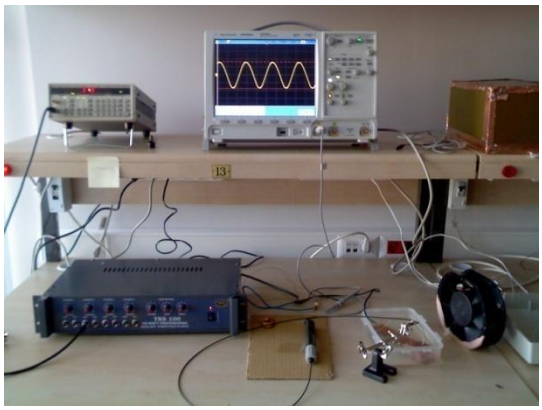

Figure 4.1.4- Overall setup for tissue experiments

# 4.2 LASER EXPERIMENTS

## 4.2.1 HAND FAN DESIGN

In Chapter 2, we have discussed whether it was possible to obtain half spherical lesions using three laser fibers in the orientation given in Figure 2.1. Our simulation results show that, in our proposed orientation, it is possible to obtain almost half circular lesions in the plane of incidence and narrower but deeper circular lesion in perpendicular plane. To verify this, we designed a plastic holder to hold the fibers and emit light in the desired angular orientation.

Since the fibers are too sensitive to physical contractions, especially at the tip one should be very careful when placing and mounting them to the holder. Because, in the simulations, Gaussian beams were assumed to exit the fiber core. If any damage happens to the tip, the beam may spread and the design may give undesired results.

The hand-fan design is a preliminary work to show it is possible to get half spherical lesions as it is in the simulation results. More suitable designs are considered either. The experimental setup is given in the figures below. In Figure 4.2.1, each part is drawn separately to understand the interconnections in between. However, Peltier cooler's connection is somewhat different. In above figure, only the necessary voltage level between reference nodes is shown. Yet, Peltier cooler is also connected to the temperature controller, which has a sensor connected to the metal plate. The threshold level is adjusted so that whenever temperature at the sensor exceeds 24 C, Peltier cooler starts to transfer heat from the metal plate to the cooling plate. The connections between cooler and the temperature controller are shown in Figure 4.2.2.

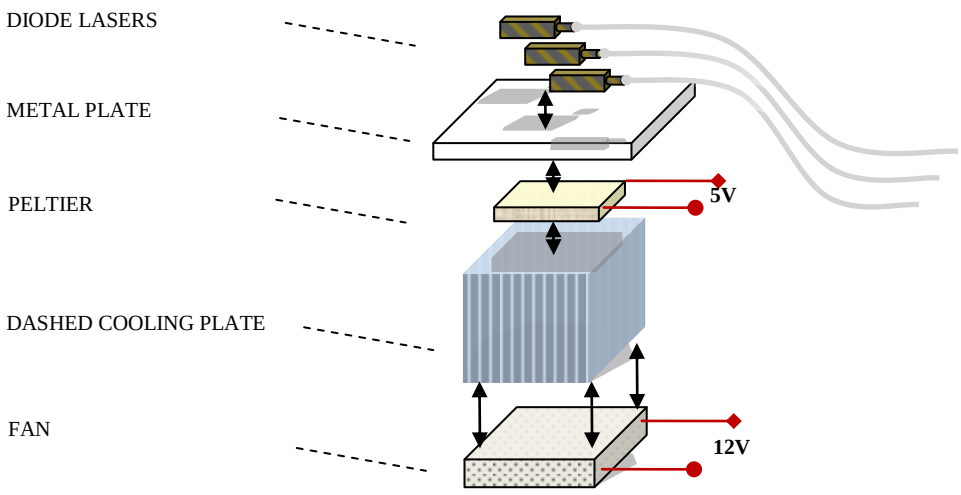


Figure 4.2.1 – Laser setup stage 1 - 976 nm Diode Lasers and cooling apparatus. The diodes are mounted diagonally for the ease of screwing purposes due to the limited space on the metal plate.

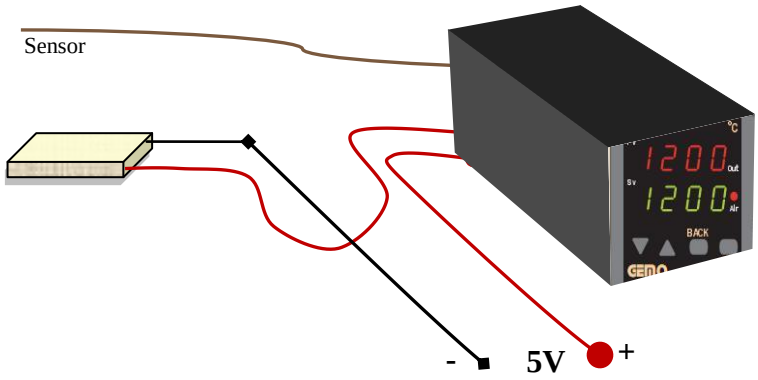


Figure 4.2.2 – Peltier cooler and temperature controller connection – Image is taken from "http://www.gemo.com.tr/"

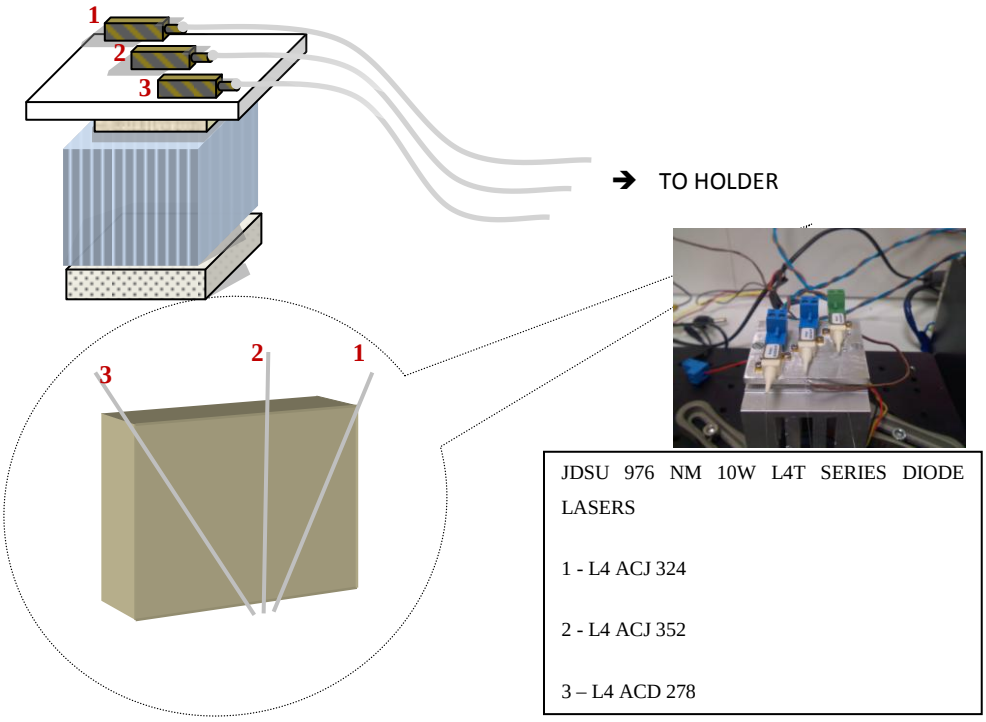


Figure 4.2.3 - Lasers and the plastic holder. The red numbers indicate which diode laser is connected to which side. The 1 and 3 are rotated 45 degrees to the left and right from number 2

#### 4.2.1.1 GEL EXPERIMENTS

The three CW (continuous wave) diode lasers (JDSU 976 nm 10W L4T Series) are connected to each of the parallel outputs of the DC power supply (Delta Elektronika S280 280 W DC Supply). Each diode laser can dissipate max 10W power. For calibration purposes and also to understand in what region we are in the data sheet showing power – current relations, one parallel branch, connecting one of the DC supply outputs to one of the lasers, is cut and a current meter is connected in series. Since the three diodes are identical, measuring the current in one branch is enough to understand in what region we are for thereof the lasers. The small differences in the fluctuations in the currents have not much importance since they do not contribute much to the intensity of the laser beam. The power intensities of the diodes are measured via optical power meter (Melles Griot Power/Energy Meter BPEM001). Instead of measuring the current, first, the voltage across the terminals of the diodes are measured at some specific levels. For each voltage level, power meter is used to measure the power intensities at the tip of each fiber. A voltage – power relation table is prepared so that by increasing the voltage level, we could understand at what power level we are in.

| | POWER (W) | | |
|---|---|---|---|
| Voltage (V) | Laser # 3 | Laser # 2 | Laser # 1 |
| 1.359 | 0.037 | 0.080 | 0.110 |
| 1.397 | 0.560 | 0.750 | 0.780 |
| 1.414 | 0.810 | 1.100 | 1.100 |
| 1.443 | 1.298 | 1.563 | 1.421 |
| 1.470 | 1.606 | 2.180 | 2.200 |
| 1.500 | 2.200 | 2.850 | 2.800 |
| 1.510 | 2.500 | 3.190 | 3.220 |
| 1.525 | 2.750 | 3.600 | 3.600 |
| 1.540 | 3.050 | 3.990 | 4.010 |

Table 4.2.1 – Voltage and Power Relations for parallel connection

After measuring the power up to 4W, which is well below the maximum power that the diodes can tolerate, the fiber tips are mounted to the plastic holder. It should be noted that the laser tips should be cut well and cleaned after slipping off the outer protection. The wiping process is done with the help of a sensitive tissue and Propanol. The cutting is done via a fiber cleaver. At the same voltage level, diode#3 have less power at the fiber tip. This is due to the splicing of the diode's original fiber extension with another fiber, prior to the experiment. When it is realized with IR camera that, at the junction, there is power loss because the junction appears to emit light, which means light is not trapped well in the core. However, the splicing at the junction was not changed intentionally to see the effect of this less emission on the gel.

To compare this experiment with RF ablation gel experiment, temperature sensor is again used. As opposed to the RF experiment, in here, 2 channels of the sensor are used. The temperature sensor tips are together placed at both the posterior and the anterior positions of the holder as seen in the Figure 4.2.4.

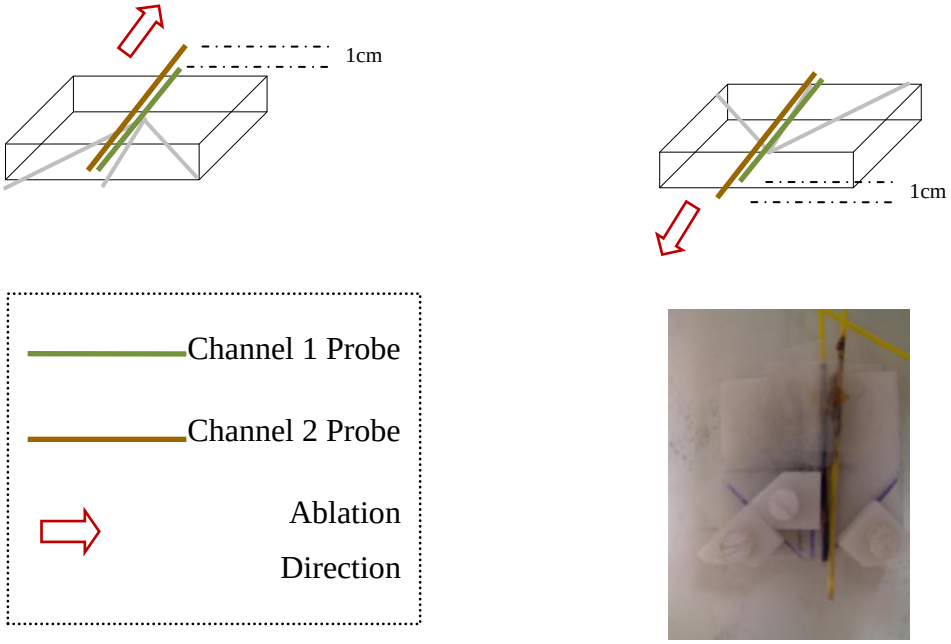


Figure 4.2.4 - Fiber and temperature probe positions on the holder - (Above Left): temperature probes are installed at the anterior part of the holder where the fibers are at the posterior side – (Above Right): Both the temperature probes and the fibers are installed at the anterior part of the holder - (Below Right): The picture of the above right figure

Then, the holder is aligned over the gel phantom as seen in Figure 4.2.5. one is touching the surface of the gel and the other is away from the surface by 0.6 cm. Two experiments are conducted for this step by applying 1.470 V to each diode (Total optical power of 6W for 30 seconds).

#### 4.2.1.2 TISSUE EXPERIMENTS

The laser system and holder used in the tissue experiments are just the same as they are in the gel experiments. Besides, the connections between the pump diodes and the DC supply were altered. In gel experiments, to be able to adjust the currents passing through the diodes separately, the interconnections were made parallel. If we had desired to decrease the current in one branch to alter the lesion shape, we could have connected a series variable resistor to that branch. However, after conducting the experiments on gel phantoms, by applying the same amount power for each branch, we were able to create the desired lesions as will be seen in Chapter 5. So, to be able to use diodes more efficiently, the interconnections were replaced with series ones and current – power related calibrations are done. The calibration results are given in Table 4.2.2.

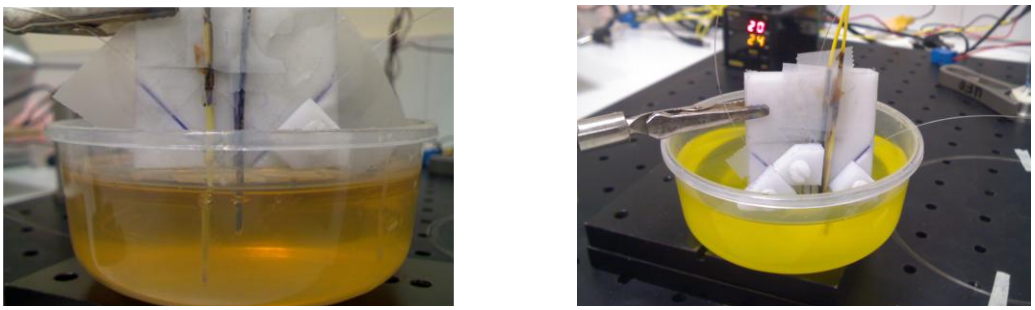

Figure 4.2.5 - Fiber and temperature probe orientations over the surface of the phantom

| | POWER (W) | | |
|---|---|---|---|
| Current(A) | Laser # 3 | Laser # 2 | Laser # 1 |
| 1 | 0.428 | 0.498 | 0.443 |
| 1.25 | 0.622 | 0.734 | 0.671 |
| 1.5 | 0.818 | 0.975 | 0.909 |
| 2 | 1.267 | 1.403 | 1.390 |
| 2.2 | 1.420 | 1.679 | 1.525 |
| 2.5 | 1.706 | 1.986 | 1.854 |
| 3 | 2.08 | 2.46 | 2.31 |
| 3.5 | 2.54 | 2.90 | 2.72 |
| 4 | 2.98 | 3.40 | 3.16 |
| 4.5 | 3.36 | 3.90 | 3.71 |

Table 4.2.2 – Current and Power Relations for series connection

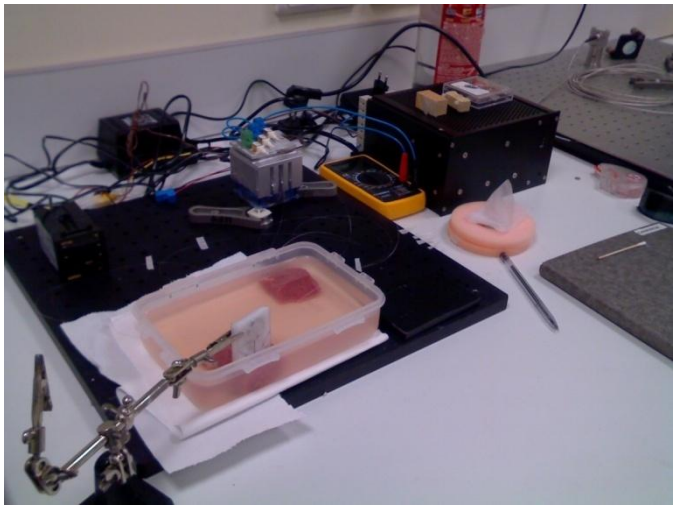

Figure 4.2.6 – Overall setup for laser tissue ablation with hand-fan design

After calibrations are done, the tissue (beef – cow meat) is put in a plastic transparent box filled with water and the laser holder is fixed upon it. The orientation and overall setup is seen in Figure 4.2.6. The lesion is formed by applying each diode 3A current for 1.5 - 2 minutes. Total optical power delivered to the tissue is 6.85W by looking at the 7$^{th}$ row of Table 4.2.2. As to control whether the width of the lesion is due to the heat convection or absorption related heating, also, 2 fibers (#3 and #2) are positioned perpendicular to the tissue with the help of the holder. To be able to deliver the

same amount of energy, diodes were driven with 4.5A current for 1.5 - 2 minutes. The burns are then compared.

### 4.2.2 AIR GLASS INTERFACE DESIGNS (LENS DESIGNS)

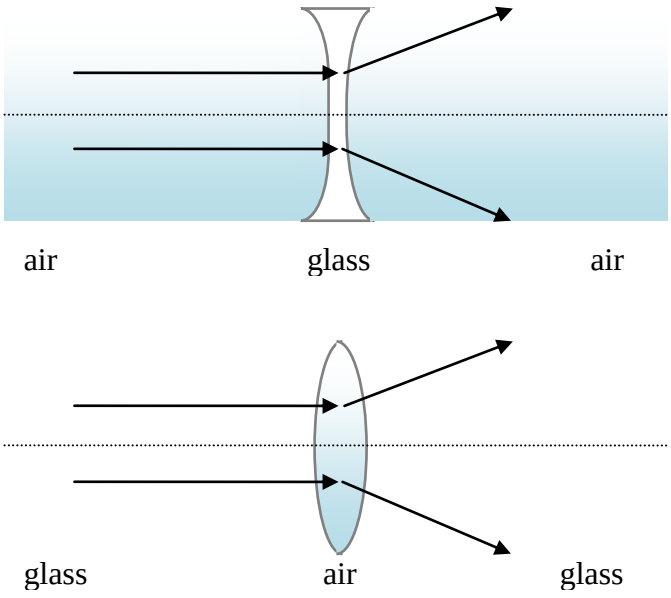


Figure 4.2.7 – Refraction between different media

The dimensions of the hand-fan design are not suitable for interventions. Besides, it was only used to understand whether it is possible to form RF like burns. In this section, an insertable design is going to be discussed.

According to the Snell's Law, when light passes from one medium to another with different refractive indices, it refracts in the plane of incidence obeying the refraction rule:

$$n_1 \sin\theta_1 = n_2 \sin\theta_2$$

where, $n_1$ and $n_2$ are refractive indices of the media accordingly and $\theta_1$, $\theta_2$ are the angles of the rays with the normal.

Since we are working with glass fibers, we have three media, which are gel phantom (or tissue), glass fiber and air. So, we need to be interested in three different refractive indices. However, at our wavelength (976 nm) the refractive index of the mammalian tissue is in between 1.35 – 1.55 [45]. Before using any mammalian tissue, we conduct our experiments on gel phantoms. We assumed its index of refraction around equal to water, which is 1.33.

We assumed three media as fiber (glass), air (lens), tissue or gel (glass). In Figure 4.2.7, above configuration; the interfaces are air - glass and glass - air. Where $n_{air}$ = 1 and $n_{glass}$ = 1.460 (fused silica) and $n_{gel}$ is assumed in between 1.33 – 1.4. The parallel light coming through the air is refracted and widened after passing through a biconcave lens. However, in our design the order of the media is different. The beam coming through the fiber first comes across with the air medium and then, it is assumed to pass through the gel (assumed as glass). Since we desire spherical lesions, we need homogeneous spherical refraction at the interface. This can be obtained by air bubble, or a glass sphere filled with air. In other words, to obtain the same light refraction behavior in Figure 4.2.7 up, we need to put a convex air lens at the interface.

The curvature of the lens is very important. Since the beam is not collimated, instead of following a straight path, it bends towards the sides after exiting the fiber. This is what we desire before refraction at the interface. Whenever the uncollimated beam reaches the interface, it refracts and diverges more from the media axis. If the curvature of the air – glass interface is too low, the rays coming from the fiber do not refract more, since they are almost parallel to the interface normal as seen in Figure 4.2.8.

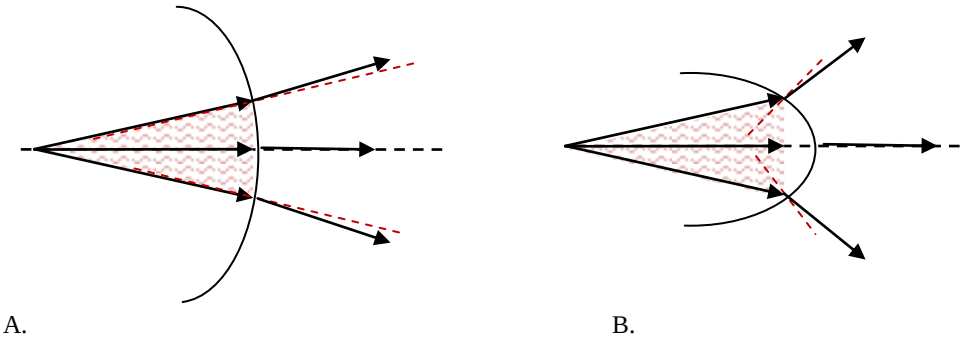


Figure 4.2.8 - The behavior of the uncollimated light. A. Behavior at the interface with lower curvature B. Behavior at the interface with higher curvature

When we put the interface at a suitable distance that the beam divergence is much enough to spread the light, then we are going to have enough and homogeneous refraction to crate half spherical lesions. To do that, the thinnest capillary and pastor tubes those are available in medical market are used and crafted at a glass workshop. The micro tubes have inner radius of 750μm and outer radius of 1000 μm. To get an air – glass curved interface, the glass tubes are molten and by inflating them at high temperature, air filled glass bubbles are formed at various diameters. However, as will be clearly seen from experimental results, the lower curvature bubbles are not suitable for intense refraction as also seen in Figure 4.2.8.

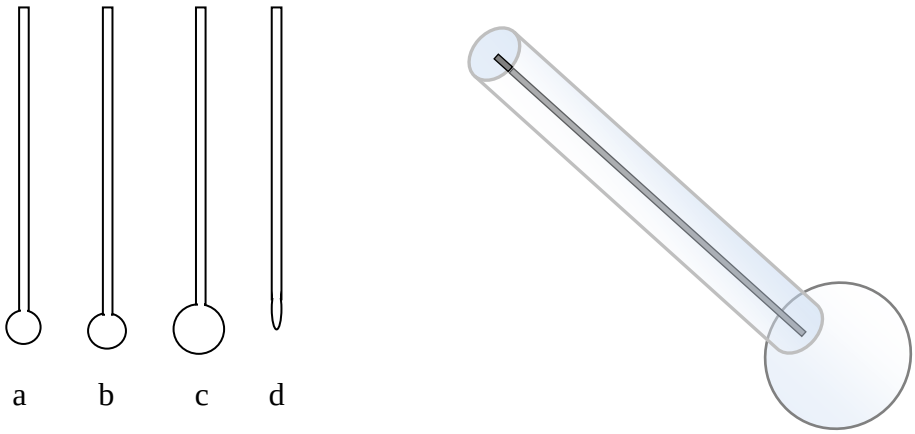


Figure 4.2.9 - The glass micro bubble ended tubes through which the fibers are passed. Diameters of the ends are a) 1.5mm b) 2mm c) 2.5mm d) <1mm

#### 4.2.2.1 GEL EXPERIMENTS

For this part, the setup in Section 4.2.1.1 is used, in which the diodes are connected in parallel. Before trying the glass tubes on gel phantom, to see where the light reaches after the refraction at the interface, the fiber is inserted into the micro bubble ended tubes and the tube is dipped into water. The refracted light is followed with an IR camera and IR viewing card at the surface of the water filled glass. The best refraction is seen when we used such a curvature as in Figure 4.2.8B and Figure4.2.9 d.

Having checked which one of the glass tubes refracts more light with the IR card, each tube with fiber inside is submerged into the gel. The experimental setup is just the same as our "Hand-Fan" design setup, where, only diode#2 is used and others are bypassed. For design (d) the diode is driven with 1.540V for 5 minutes. Two lesion shapes are investigated after $1^{st}$ and $5^{th}$ minutes. The corresponding power value is 4W from Table 4.2.1. For design (a) same power level is adjusted and lesion shape after $1^{st}$ minute is investigated. The results are given in Chapter 5.

#### 4.2.2.2 TISSUE EXPERIMENTS

For this part, the setup in Chapter 4.2.1.2 in which the diodes are connected in series, is used. As in gel experiments the designs (a) and (d) are mounted. Fiber # 2 is inserted into the designs and the diode is driven with 5A for 4 minutes (4.5W) for both designs. The results are given in Chapter 5.

### 4.2.3 VERIFICATION OF LESIONS BY USING MR THERMOMETRY

MRI has the ability to construct in vivo body temperature maps. These maps are useful for image guided interventional thermal therapies. For our purpose, thermal maps of the ablation zone can be constructed to relate the absorption dependent simulation results with thermal maps.

To obtain MR thermometry maps during ablation of gel or tissue phantoms, PRF (proton resonance frequency) method was used with a similar approach as in [53]. The main principle of this method is based on the de-phasing of heated molecules. For example, water molecules slow down with the rate of approximately 0.01 ppm per $1^{o}$C temperature rise. In other words, PRF thermal coefficient of a water molecule is -0.01 ppm/$^{o}$C (ppm: parts per million).

To be able to obtain thermal maps, one needs to measure a reference temperature from a thermally insulated part of the phantom. Then, this value should be used to compensate MR phase drifts. All MR imaging was done with a 3T Siemens Magnetom Trio inside a head matrix. GRE (TR = 80ms, TE = 20ms, number of slices = 5 with data acquisition time of 5.25 sec/3slices, 200 Hz-px BW with a measurement number of 40) sequence was applied for both gel and tissue phantoms. Only the phase images are considered to obtain thermal maps.

The experimental setup is given in Figure 4.2.10 and 4.2.11. Two MATLAB based codes were implemented and executed on Terminal PC for both real time (5.25 sec/slice) and post processing of phase images. The program considers first 10 phase images as reference images, since up to the $10^{th}$ measurement (52 seconds), no laser delivery was given. Then, the arithmetic mean of each corresponding pixel of these 10 images was taken and a

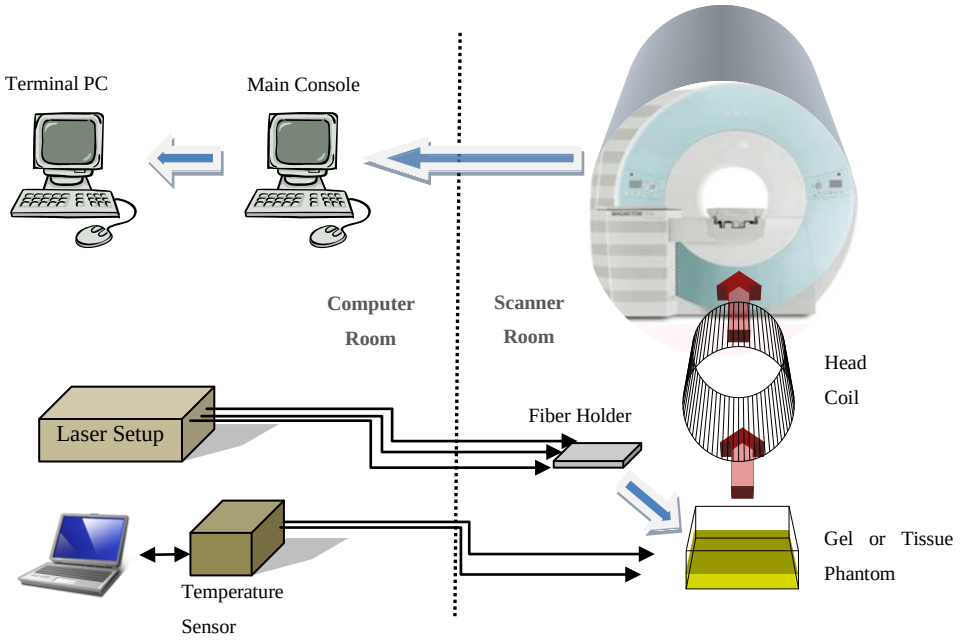


Figure 4.2.10 – Experimental setup for MR thermometry verification

reference phase image $\Phi_{base}(x, y)$ was constructed. The laser was switched on and ablated the phantom with 9.56 W for 158 seconds.

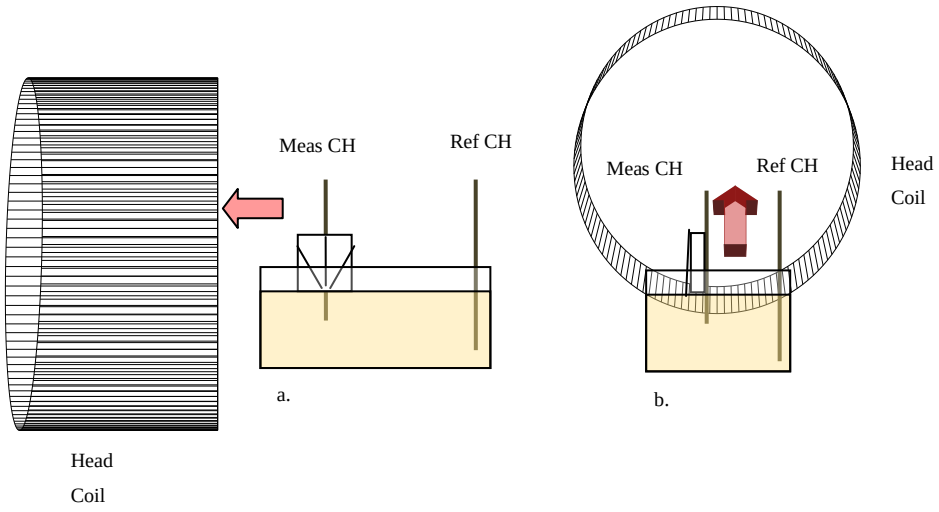


Figure 4.2.11 – Fiber and temperature probe orientation a. Front view b. Side view

The general equation relating the phase difference with temperature rise is given below:

$$\Delta\Phi(r,t) = \alpha\,\gamma\,B_0\left({}^{360^o}/_{cycle}\right)TE\,\Delta T(r,t)$$

where

$B_0$ ; main magnetic field strength

α; prf thermal coefficient

γ; gyromagnetic ratio

TE; echo time

ΔΦ; phase difference between reference image and the image in progress

ΔT; Corresponding Temperature change

The detailed flowchart of the program is given in Figure 4.2.12. Since we are working with DICOM images (where the phase values of the pixels have integer values), each image in progress are scaled in between –π and π. Then, exponentials are taken to make each pixel a complex value. The magnitude of each pixel then becomes 1, which does not affect our progress, since temperature rise is related with phase difference (angle), not with the magnitude of the pixel. After forming $\Phi_{base}(x,y)$ , each new complex image is multiplied with the complex conjugate of $\Phi_{base}(x,y)$ and the angle of this multiplication is calculated ($\Phi_i(x,y)$). Then, the phase drift compensation is done as follows:

$$\Phi_i(x,y) = \Phi_i(x,y) - \alpha\,\gamma\,B_0\,(360^o/\text{cycle})\,TE\,\Delta T_{ref}$$

After this step, phase unwrapping is done by comparing two consecutive images. If the difference of each consecutive pixel ($\Phi_i$ (x,y) and $\Phi_{i+1}$ (x,y)) is greater than π or smaller than -π, 2π is subtracted or added to correct the phase. Then ΔT(r,t) is calculated.

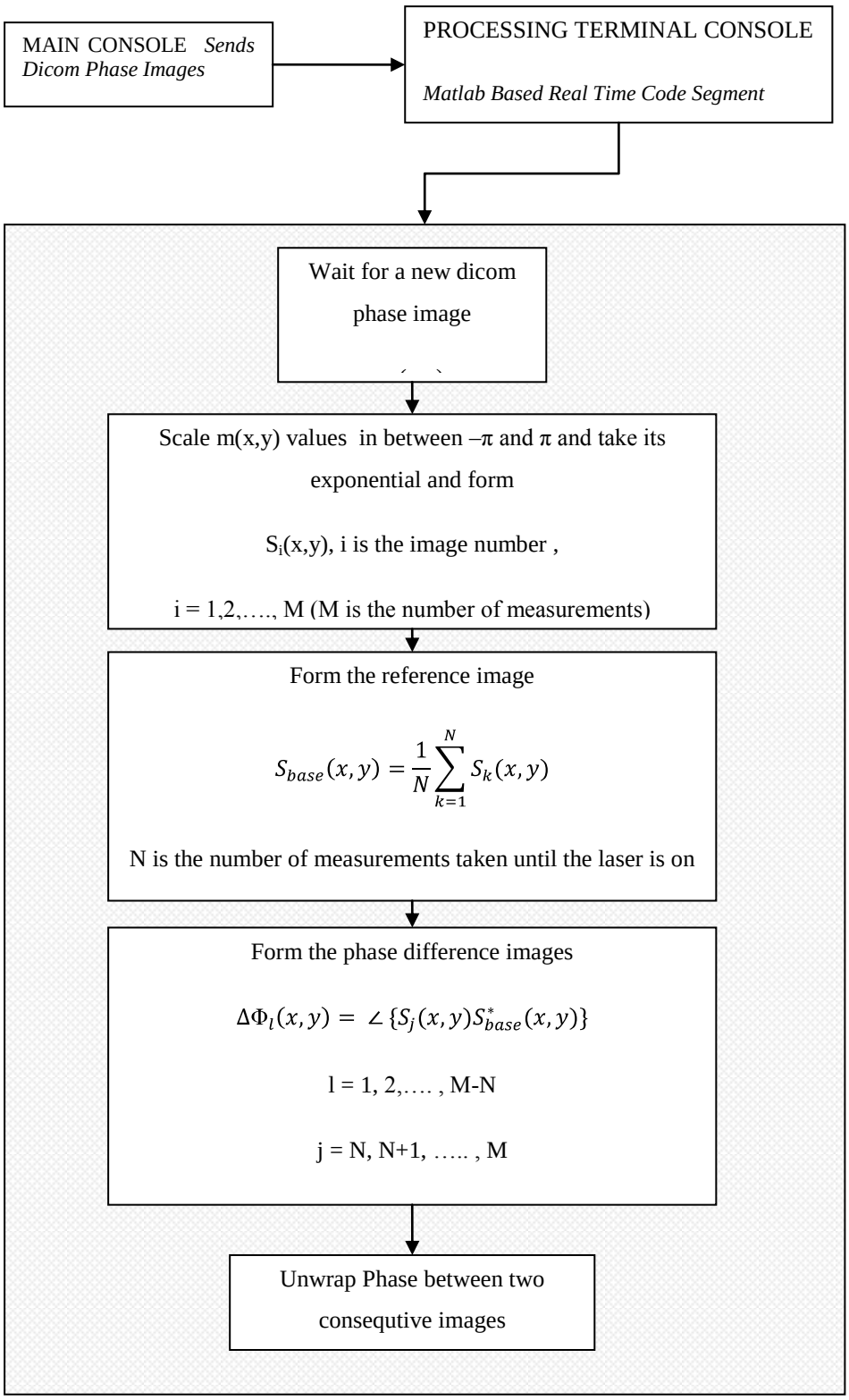


Figure 4.2.12 – Flowchart of the Program

# CHAPTER 5

# RESULTS

## 5.1 SIMULATION RESULTS

In this section, the combined 2D and 3D MCML and MATLAB results for SAR distribution of single fiber and three fiber scheme (hand-fan design) of Figure 2.2 will be shown.

The both two dimensional and three dimensional absorption distributions are shown in the figures below. 2D absorption distribution for single fiber excitation is seen in Figure 5.1.1.a. The absorption pattern seems deeper than it's wider. Each pixel corresponds to 125 μm length. So, the SAR pattern has a length of 2.5 mm (20 pixels) and 1.25 mm (10 pixels). The depth to width ratio of the SAR pattern is 2. $45^{o}$ and $-45^{o}$ inclined fiber excitation results are seen in Figure 5.1.1.b and 5.1.1.c. Overall 2D circular pattern (SAR region created with hand-fan design) can be clearly seen in Figure 5.1.1.d. The depth to width ratio is now 0.83 (20 pixels/ 24 pixels).

Figure 5.1.2 shows 3D contour plot of the absorption pattern of single fiber excitation, where, Figure 5.1.3 shows the 3D contour plot of the absorption pattern of the hand-fan design. In Figure 5.1.4 the 3D simulation of inclined fiber orientation is given. The slice in xz plane (refer to the Figure 2.1) of the 3D simulation is given in Figure 5.1.5. Note that this orientation is the same as 2D view in Figure 5.1.1.d. So, it has the same depth to width ratio, which is 0.83. On the other hand, pattern in zy plane has narrower width (Figure 5.1.6). This was expected since the three fiber orientation is laid in xz plane. The depth to width ratio of this side view is then 20pixels/10 pixels, which is 2. This value is the same as it is in the single fiber excitation case.

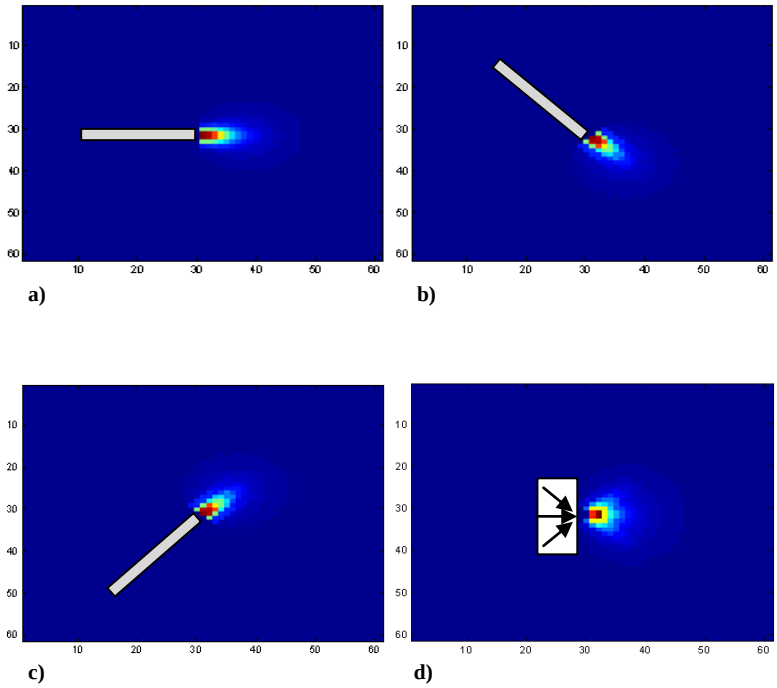


Figure 5.1.1- Two dimensional absorption distributions with respect to r and z (r - vertical axes, z - horizontal axes). (a) Perpendicular fiber orientation to the tissue. (b) Fiber is rotated by 45 degrees on the rz plane. (c) Fiber is rotated -45 degrees on the rz plane. (d) Sum of a,b and c (Hand – Fan).

Note: Intensities of the pixels are not considered since the desired absorption distribution has priority.

In the simulations, no result for the intensity of the absorption distribution was considered, since it was the priority to gel a half circular SAR pattern in the plane of excitation.

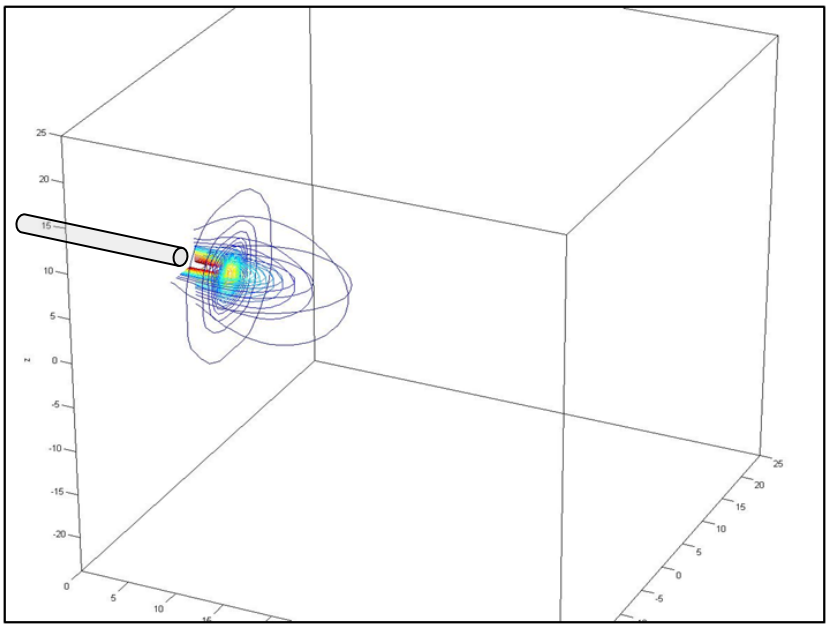

Figure 5.1.2 – Three dimensional contour plot of absorption with single fiber excitation. The orientation of the fiber is shown with grey cylinder.

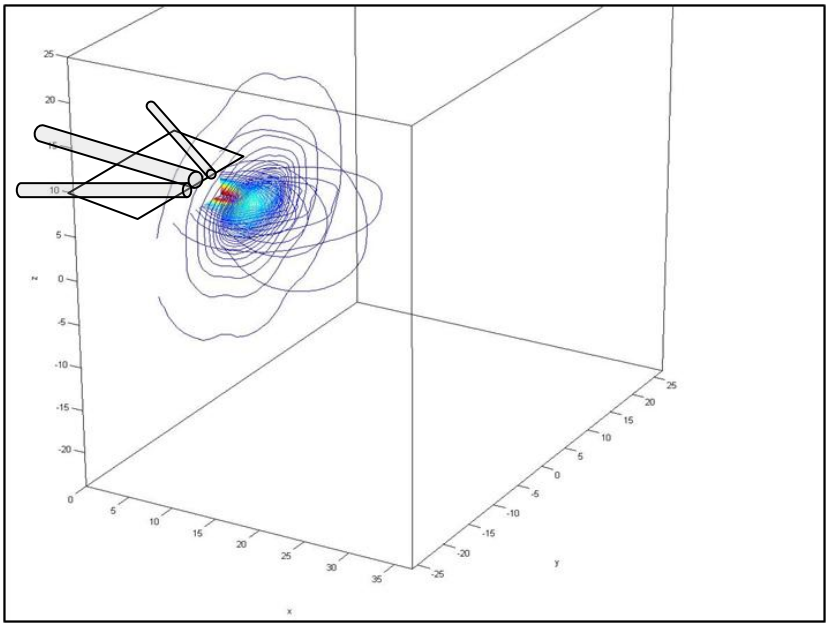

Figure 5.1.3 – Three dimensional contour plot of absorption with the design given in Chapter 2. The orientation of the fibers and the excitation plane are shown with grey cylinders and white plate.

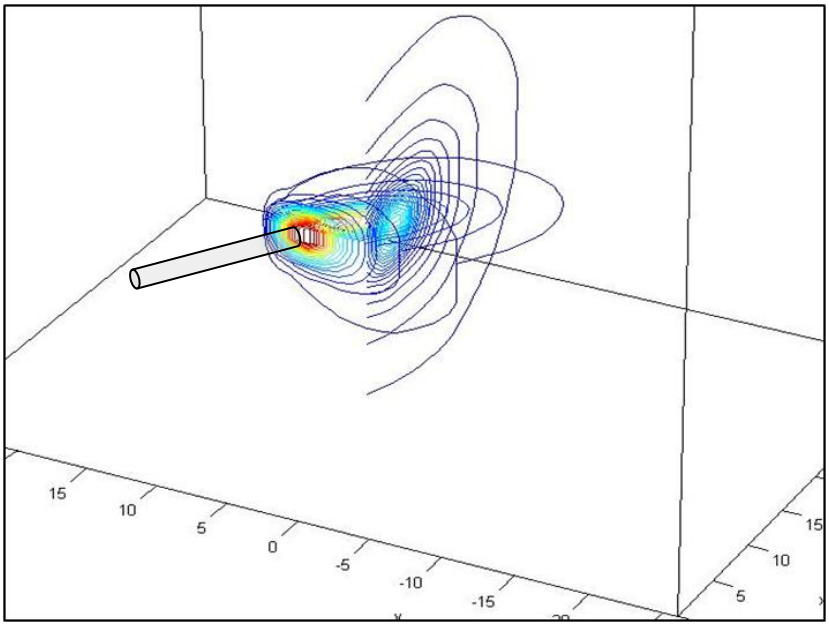


Figure 5.1.4 – Three dimensional contour plot of absorption with inclined single fiber excitation. The orientation of the fiber is shown with grey cylinder.

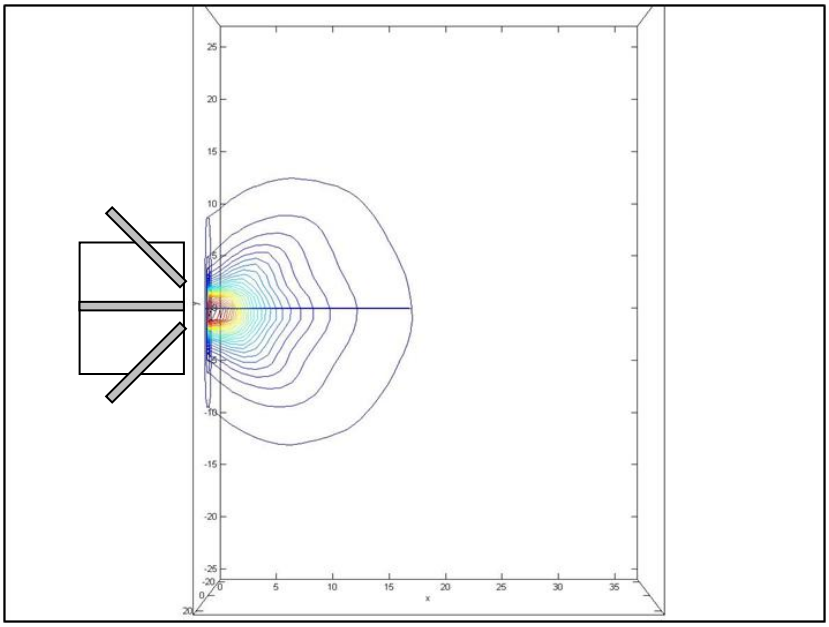


Figure 5.1.5 – Three dimensional contour plot of absorption with the design given in Chapter 2. The orientation of the fibers and the excitation plane are shown with grey cylinders and white plate. (Top View)

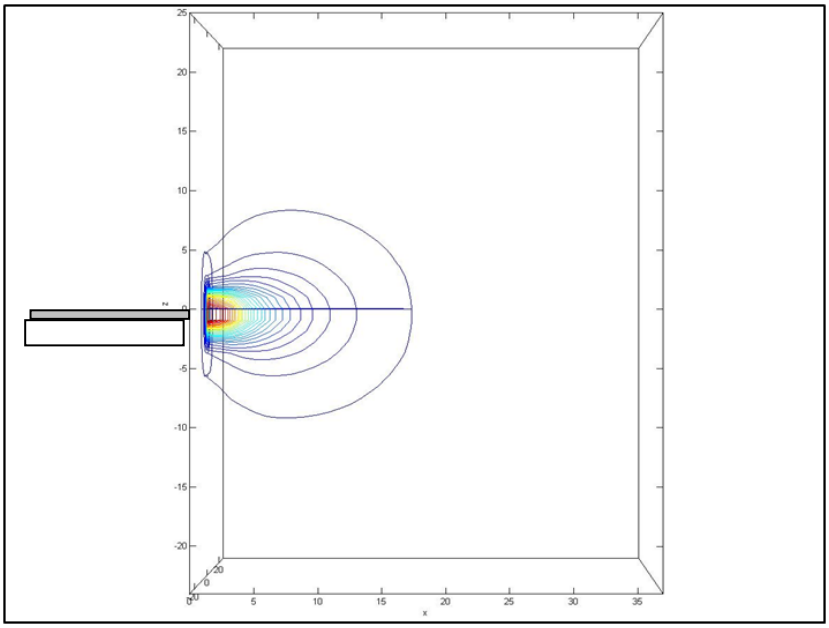

Figure 5.1.6 – Three dimensional contour plot of absorption with the design given in Chapter 2. The orientation of the fibers and the excitation plane are shown with grey cylinders and white plate. (Side View)

## 5.2 RF EXPERIMENT RESULTS

In the simulations, whether a circular absorption region can be obtained in the plane of three fiber design was investigated. Since the absorption patterns of laser system and RF system cannot be compared directly, which was described in Chapter 2, it is better to compare the temperature distributions, or lesions sizes created by them. In this section, experimental results of RF probe tissue or gel interaction is investigated, as it is our comparison criterion. For gel experiments, a temperature probe is also inserted in various locations to observe the heat convection effect. This is done to get an insight about how the temperature gradients behave. The size of the melted region and burns formed inside the tissue are noted.

### 5.2.1 RF GEL EXPERIMENT RESULTS

For about 30 seconds, no deformations occurred inside the gel. After 40$^{th}$ second, deformations started to occur as half spherical lesions. Then, the shape is preserved, but the dimensions increased. The initially formed shape is assumed to be the impulsive response of the system. It is understood that, the heat convection occurs through this impulse response to the outer diameters with almost half spherical gradients. Even the lesion shapes are almost the same, including their size, the measured temperatures differed. Measured temperatures are given in Figure 5.2.1, where, Figure 5.2.1.a and Figure 5.2.1.b are obtained by applying the same amount of power for different durations. After the burns were made, a ruler was dipped into the gel and the size was measured, where, the boarders of the melted region can be seen clearly. The burns that are formed inside the gel were all spherical with the width and depths given in Table 5.2.1. As it is seen from the table, all the melted regions are wider than they are deep.

| Power (W) | Duration (s) | Width (cm) | Depth (cm) | Depth / Width |
|---|---|---|---|---|
| **0.7** | 90 | 0.9 | 0.4 | 0.44 |
| **0.7** | 200 | 1 | 0.5 | 0.5 |
| **1** | 140 | 1 | 0.5 | 0.5 |

Table 5.2.1 - Deformation sizes with respect to duration and power for gel phantom.

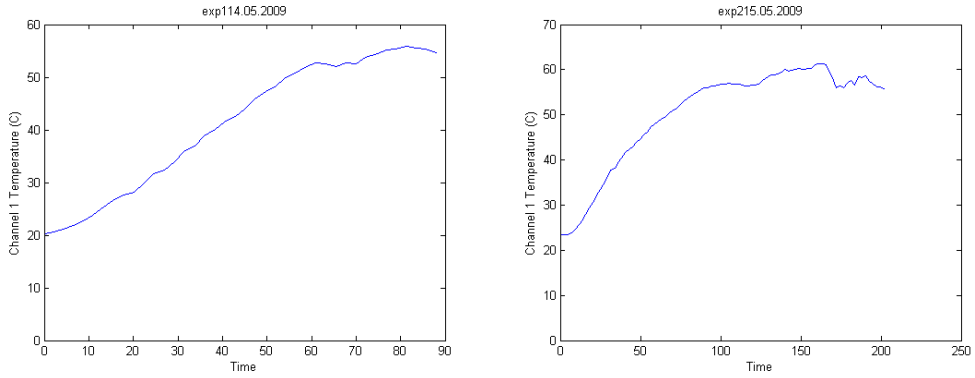


a)




b)

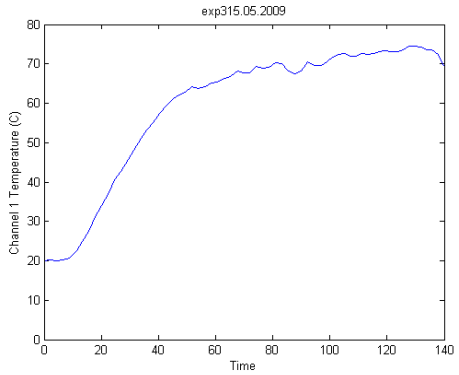


c)

Figure 5.2.1 – Temperature graphs showing the rise of temperature of the gel phantom around RF electrode. (a) Temperature sensor is 2 mm away from the electrode through the surface and at the same level with the electrode through the depth. Delivered power is 0.7 W (b) Temperature sensor is attached to the electrode and they are at the same level through the depth. Delivered power is 0.7 W (c) Temperature sensor is attached to the electrode and they are at the same level through the depth. Delivered power is 1W

## 5.2.2 RF TISSUE EXPERIMENT RESULTS

After 17.5 W delivery of power to the tissue for 1 minute, transversal and longitudinal slices are cut through the middle of the scar. The observed lesions have 0.8 cm width and 0.5 cm depth (wider than it is deeper), with a depth to width ratio of 0.63.

Figure 5.2.2 – The lesion formed after 17.5W 1 minutes of RF delivery. (Left) Transversal slice. (Right) Longitudinal slice.

## 5.3 LASER EXPERIMENT RESULTS

To compare the laser burn sizes and shapes with RF ablation burn's, hand-fan design and bubble ended capillary glass tube lens interface designs were experimented on both gel and tissue. The depth, width, and depth to widh ratios are then compared.

### 5.3.1 HAND FAN DESIGN RESULTS

#### 5.3.1.1 HAND FAN GEL EXPERIMENT RESULTS

While measuring the temperature at the sensor positions, sudden increases are seen due to the direct laser illumination whenever the probes are placed onto the anterior part of the holder (the part where the fibers are also mounted). If we place the probes to the posterior part, it is seen that the temperature increase is slow and is up to $30^{o}$ C degrees at most. This shows that the heat convection is slow at those positions. Then, it can be concluded that there is no heating due to the absorption of the gel. In other words, at a length of the thickness of the holder, which is 0.6 cm, there is no light emission from front panel to the back panel of the holder.

The SAR, as it has the relation with the slope of the temperature curve, cannot be calculated directly from the laser experiment temperature graphs. At RF ablation, the probes measured at most $70^{o}$ C with slowly increasing slope. So, it is better that the comparison criterion should be the output powers and the lesion formations. The temperature curves are given in the figure below.

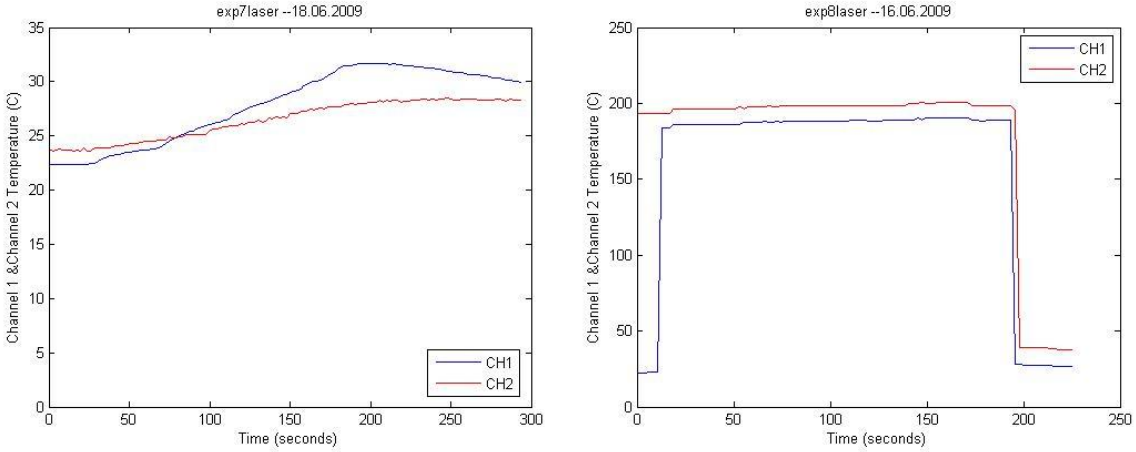


Figure 5.3.1 –Temperature graphs of gel phantom experiment with laser illumination. Left: Probes are at the anterior part Right: Probes are at the posterior part (probes are exposed to direct laser light).

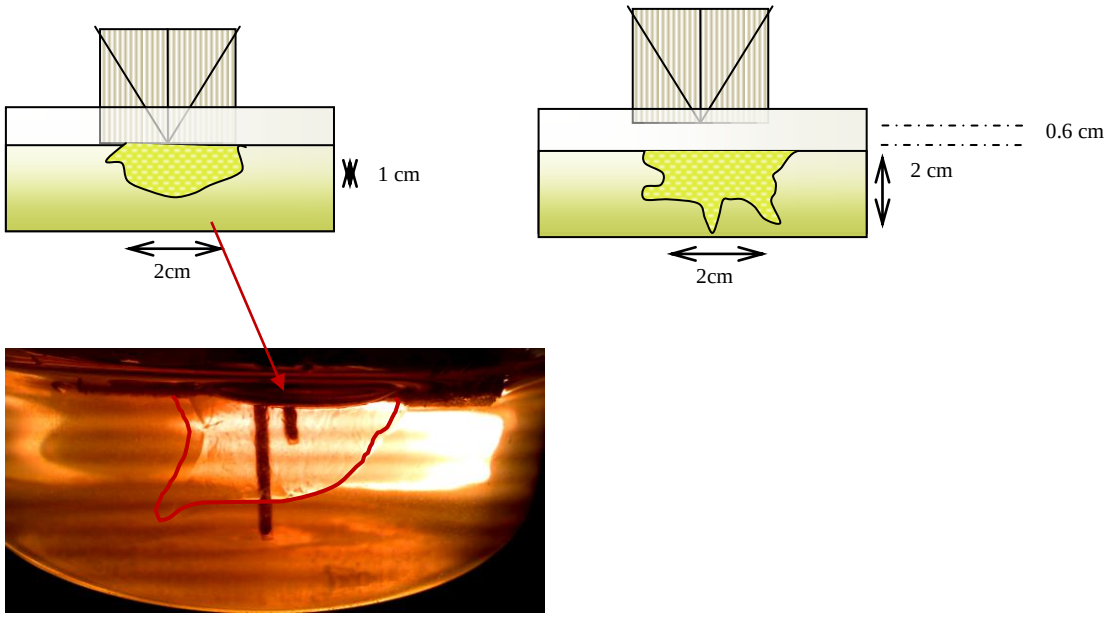


Figure 5.3.2 –Lesion formation in the gel for 6W 30 seconds delivery with hand fan design

The lesion formations for gel phantom are seen in Figure 5.3.2 for 6W – 30 second delivery of hand fan design. The melts are formed by touching the design to the gel and by leaving a gap of 0.6 cm between the gel surface and the side of the design. This was done as two consecutive experiments. The burns then said to have mean width of 2 cm and mean depth of 1.5cm, with a depth to width ratio of 0.75.

#### 5.3.1.2 HAND FAN TISSUE EXPERIMENT RESULTS

After exposing 6.8 W light illumination to the tissue for 2 minutes, the ablated lesion is cut to obtain transversal and longitudinal slices. The longitudinal slice lies in the plane of incidence (as in Figure 5.1.5.) and the transversal slice is perpendicular to the plane of incidence (as in Figure 5.1.6.). And also, it is shifted from the origin of ablation by 3mm. Since the fibers are focused at one point on the tissue, local extensive heating occurred and char was formed. However, this char formation did not affect the results, since, whenever it was formed, the laser system was switched off to prevent rapid change in the absorption or any other optical properties of the tissue. The lesion to the left is circular as expected with a width of 1 cm and a depth of 0.8 cm, with a dept to width ratio of 0.8 (orientation of Figure 5.1.5). The perpendicular slice (3 mm shifted from the origin), on the other hand, is narrower and shallower with respect to the lesion in the left and has a width of 0.4 cm and a depth of 0.35 cm.

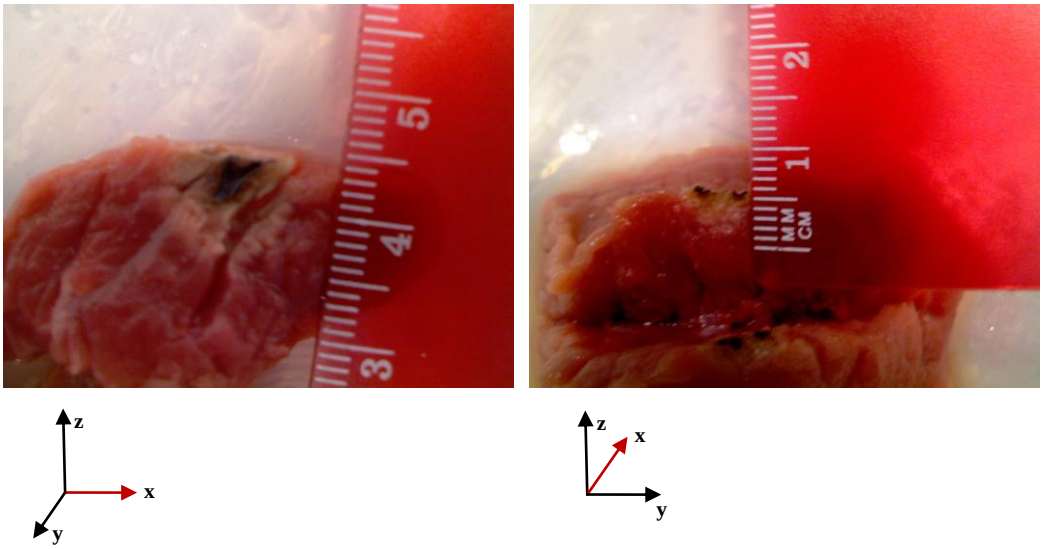


Figure 5.3.3 –Lesion formation inside the tissue for 6.85W 2 minutes delivery. Left – Hand Fan holder anterior lies in the xz plane. Right – Hand Fan holder anterior lies in the xz plane. The slice is cut 3mm from the origin of ablation.

The lesion created by the perpendicular orientation of two fibers to the surface of the tissue (with same power level with our hand fan design) is given below. Only the caption of the width of the lesion is given. It is 0.3cm where our design created a width of 1cm.

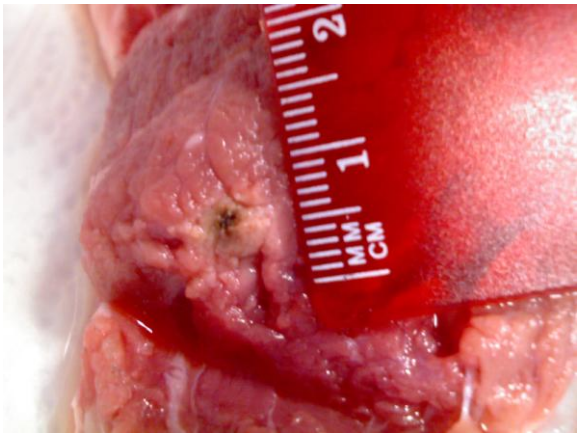

Figure 5.3.4 – Lesion excited with two perpendicular fibers (Surface view).

## 5.3.2 LENS DESIGN RESULTS

### 5.3.2.1 LENS DESIGN GEL EXPERIMENT RESULTS

The inhomogeneous light emission from the tip of design (d) can be seen in Figure 5.3.5.c (the IR camera view). The light is refracted more towards to the left of the design, due to the insensitive fabrication of the lens. Also, the melt formations are seen in Figure 5.3.5.a. b. d. e. Just after the 1$^{st}$ minute, the deformation is as it is in Figure 5.3.5.a and 5.3.5.d. The shape is not totally uniform and there seems more deformations to the left side of the lens, which supports the light emission seen in Figure 5.3.5.c. Just after the 5$^{th}$ minute, the lesion is formed as in Figure 5.3.5.b. and 5.3.5.e. The shape seems to be uniform at the regions near the tip. This is due to the uniform heat convection inside the gel, not due to the homogeneous SAR distribution. The SAR distribution is more likely to be in Figure 5.3.5.a and 5.3.5.d, because the time it takes to form such a formation is shorter than 5 minutes. The dimensions are given in the Figure 5.3.5. It is better to take the dimensions of (a), since time it takes to form such a deformation is shorter, in other words, it is where the heat convection is less effective in the formation of the melted region. The depth is 1.5 cm where the width is 1 cm with a depth to width ratio of 1.5.

Burns formed just after the 1$^{st}$ minute with design (a) is seen in Figure 5.3.6. The power is the same (4W). The tip of the glass tube seems to not to reflect the light outwards from the origin of incidence. So, the system behaves as if there is no confronting the laser beam.

For gel experiments, it is seen that lens design in Figure 4.2.9.d gives better results as opposed to design in Figure 4.2.9.a. It was expected, since the curvature of (d) is higher (Figure 4.2.8).

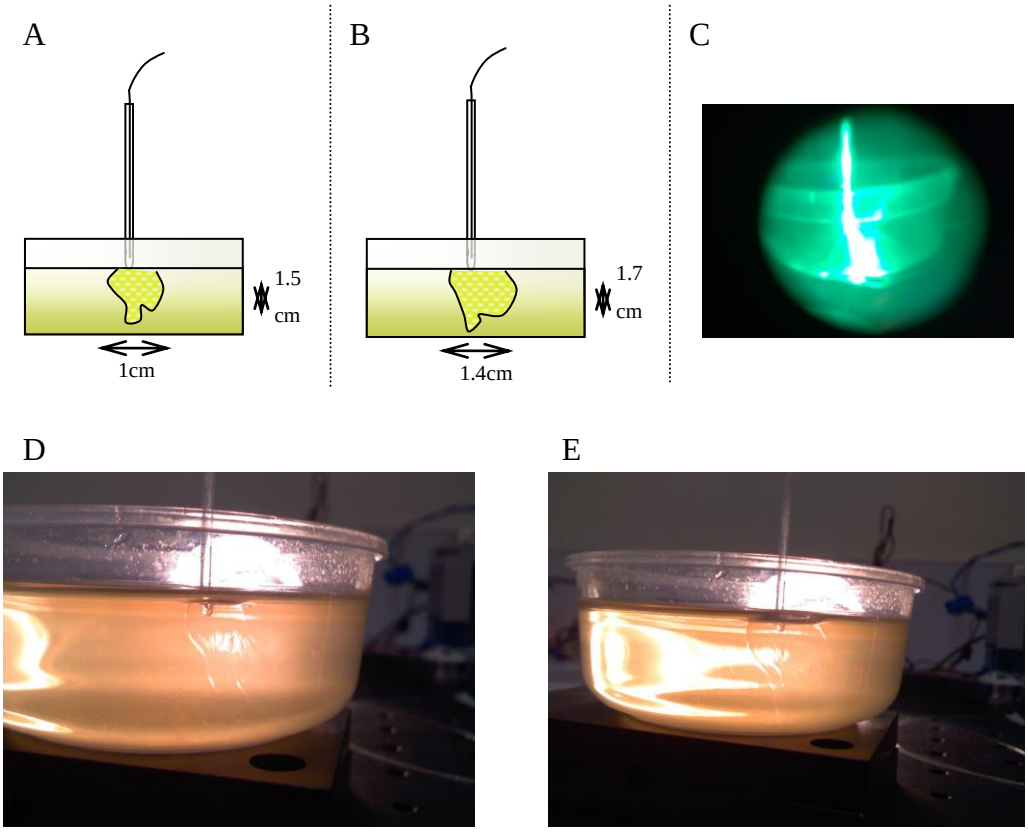


Figure 5.3.5 –Lesion formation inside the gel for 4 W with design (d). (A) – A simple scheme of the lesion just after the 1st minute. (B) – A simple scheme of the lesion just after the 5th minute. (C) - Inhomogeneous illumination due to the imperfections at the tip. (D) – Lesion just after the 1st minute. (E) – Lesion just after the 5th minute.

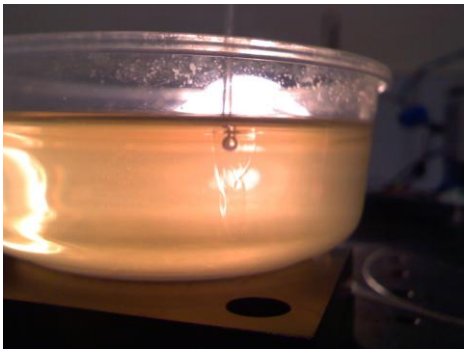

Figure 5.3.6 – Lesion formation inside the gel for 4 W with design (a). The duration of exposure is 1 min.

### 5.3.2.2 LENS DESIGN TISSUE EXPERIMENT RESULTS

After 4 minutes of 4.5 W power delivery, the lesions formed with design (a) and design (d) is given in the below figure. The lesion created with design (a) shattered since the intensity at the interface is much higher than it is in the design (d). It is understood that the part of the tissue exposed to illumination was not tight enough. There was more air underneath the surface than tissue. So, thinner tissue got more heated and exploded with design (a). With design (d), on the other hand, since the light is refracted to more than it happened in design (a) (See Figures 5.3.5 and 5.3.6), the intensity was not that much high and extensive tissue disruption did not occur.

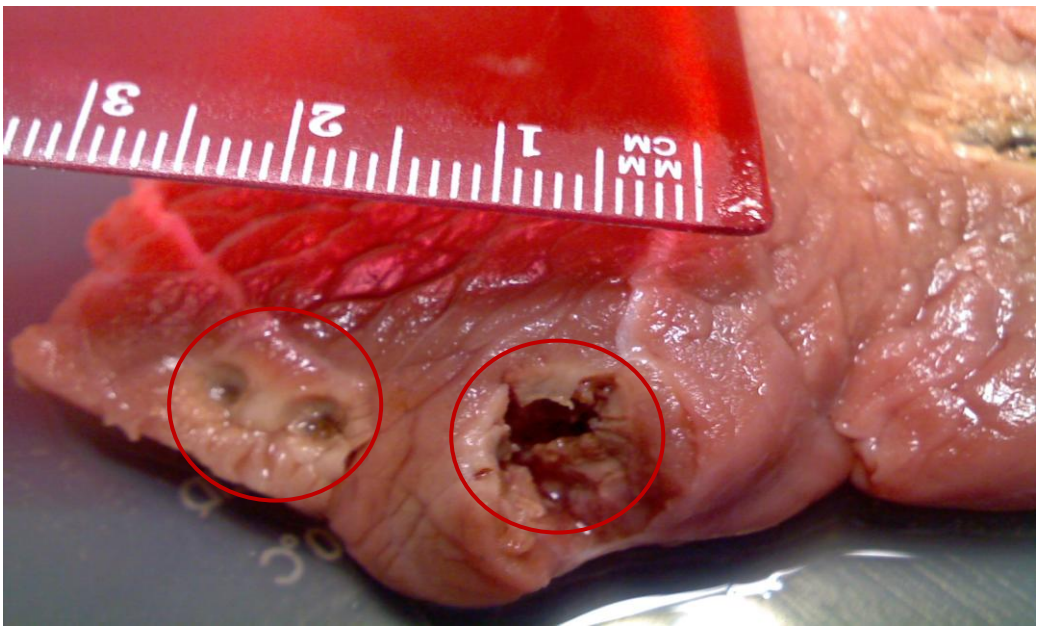


Figure 5.3.7 – Lesions after 4.5 W 4 minutes delivery of laser beam with designs (a) – right – and design (d) - left

## 5.4 MR THERMOMETRY RESULTS

As it is mentioned in Chapter 4, laser is switched off for the first 10 measurements, in other words, for 52 seconds. Then, up to 3.5 minutes, the phantom is illuminated with hand fan design. The below figures are captured at various instants. Note the similarity of lesions in Figure 5.1.5 and 5.4.1d. The temperature maps at the slice where the temperature probe is inserted are given in Figure 5.4.2. Both the probe readings and MR Thermometry values are consistent. The probe temperature reading is seen as 9.8 $^{o}$C at 157.5 seconds where MR Temperature Map shows 11 $^{o}$C and 11.3 $^{o}$C at 210 seconds where MR Temperature Map shows 12.4 $^{o}$C. Figures 5.4.1 and 5.4.2 belong to gel phantoms thermometry, where, Figure 5.4.3 belongs to tissue thermometry. The lesion formation is seen better for gel experiments. Since it is more transparent, the light reaches deeper regions. Then, a wider region gets heated and resolution becomes higher, opposed to the tissue thermometry images. Due to this fact, we are able to better observe melt formation with time. For tissue thermometry, since the resolution is lower (effective absorption length is lower), the shape cannot be distinguished well, as it is in Figure 5.4.3.c. However, the burn size can be understood.

As it is mentioned, the SAR pattern found by simulations (Figures 5.1.5 and 5.1.1.d) and the temperature distribution of the gel phantom (Figure 5.4.1) are similar. The simulations were done by considering the coefficients for tissue, where, the compared temperature map belongs to the gel phantom experiment. However, since MCML does not consider perfusion, diffusion, convection, motion etc. effects, the only difference resulting from putting gel coefficients instead of tissue coefficients would be the penetration depth, and absorption intensities. But, here, we are only considering shape. Because, as the duration of ablation is short enough, (thermal events do not take place) in a perfusionless medium, the resulting formation resembles the absorption distribution.

Each MR thermometry image has 0.9x0.9 mm pixel sizes. The temperature distribution for gel experiment at 210 seconds (after 158 seconds of ablation) has then width of 10.8 mm and a depth of 9 mm with a depth to width ratio of 0.83. The temperature distribution for tissue experiment at 210 seconds (after 158 seconds of ablation) has width and depth of 7.2 mm with a depth to width ratio of 1. The hand-fan orientations are given in the figures below.

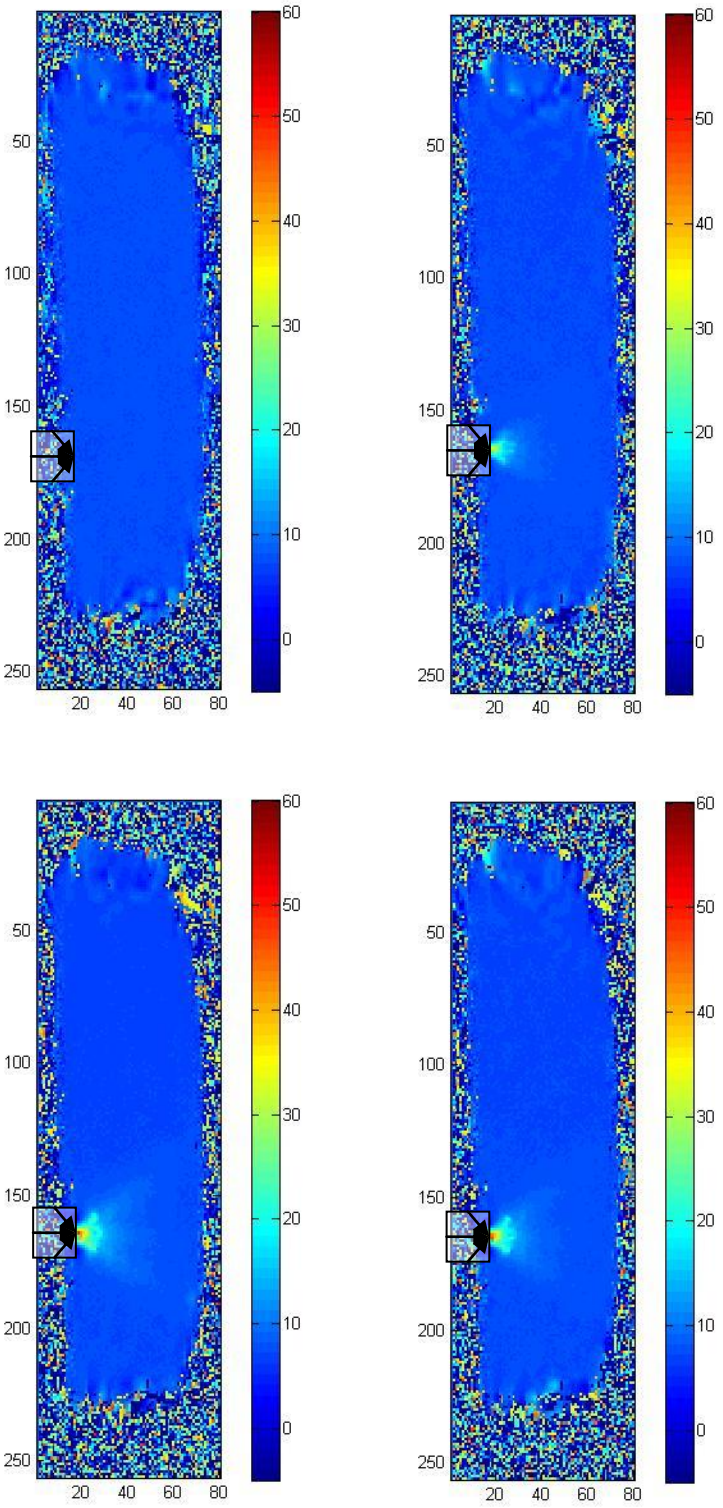


Figure 5.4.1 – MR Thermometry Images of a gel phantom a. t = 52.5 seconds b. t = 105 seconds c. t = 157.5 seconds d. t = 210 seconds

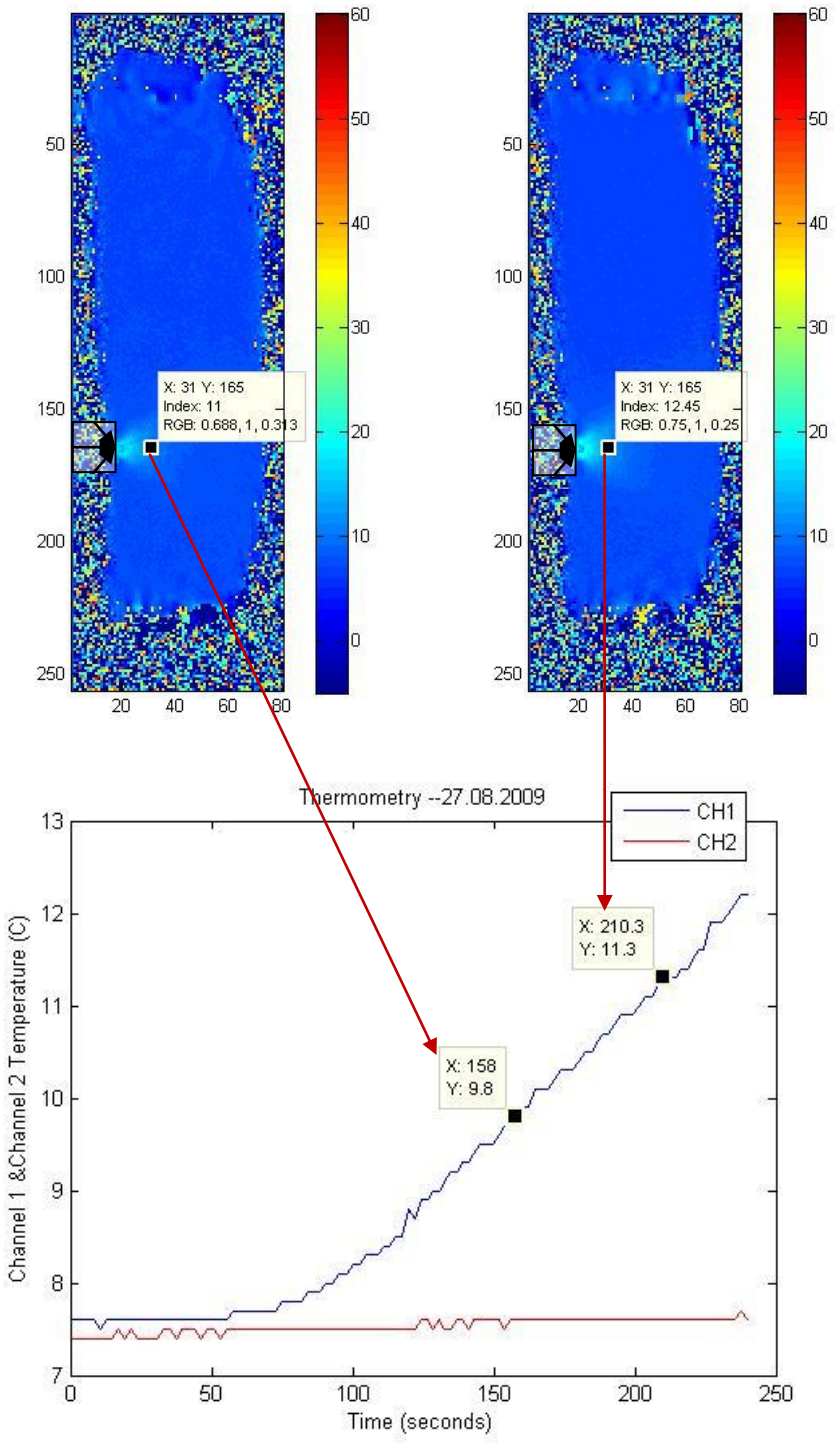


Figure 5.4.2 – MR Thermometry Images of the slice where temperature probe is inserted a) t = 157.5 seconds b) t = 210 seconds c) Temperature probe readings (CH2 is the reference temperature)

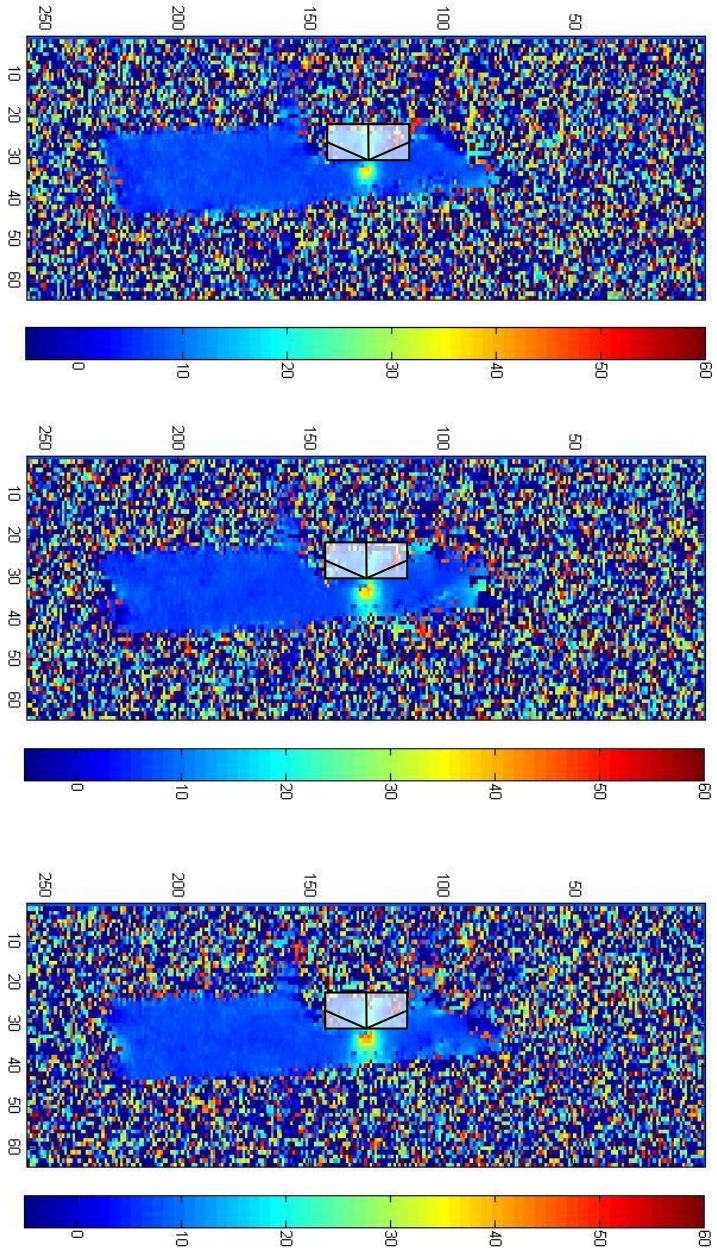


Figure 5.4.3 – MR Thermometry Images of tissue phantom. Temperature Values are given for pixel values (35,129) a) t = 105 seconds, T(35,129) = 28 $^{o}$C b) t = 157.5 seconds, T(35,129) = 32.45 $^{o}$C c) t = 210 seconds, T(35,129) = 35 $^{o}$C

## 5.5 SUMMARY

The summary of the dimensions with power duration relation for gel and tissue experiments respectively, are summarized tables below.

| Delivery Type | Power (W) | Duration (s) | Width (cm) | Depth (cm) | Depth / Width |
|---|---|---|---|---|---|
| RF | 0.7 | 90 | 0.9 | 0.4 | 0.44 |
| | 0.7 | 200 | 1 | 0.5 | 0.5 |
| | 1 | 140 | 1 | 0.5 | 0.5 |
| Hand-Fan | 6 | 30 | 2 | 1.5 | 0.75 |
| MR thermal map with hand-fan | 9.6 | 158 | 1.08 | 0.9 | 0.83 |
| Lens Design | No result is given since the lesion shape do not resemble a half circle | | | | |

Table 5.5.1 - Temperature distribution sizes with respect to duration and power for gel phantom experiments.

| Delivery Type | Power (W) | Duration (s) | Width (cm) | Depth (cm) | Depth / Width |
|---|---|---|---|---|---|
| RF | 17.5 | 60 | 0.8 | 0.5 | 0.63 |
| Hand – Fan | 6.8 | 120 | 1 | 0.8 | 0.8 |
| MR thermal map with hand-fan | 9.6 | 158 | 0.7 | 0.7 | 1 |
| Lens Design | No result is given since the optimum lesions cannot be formed | | | | |

Table 5.5.2 - Temperature distribution sizes with respect to duration and power for tissue phantom.

As it can be understood from the results, the durations and the power levels were tried to be adjusted so that the total amount of energy for every experiment have near values (max. 500J difference). For gel phantom, the increase in the temperature of a specific point is less than it is in tissue

experiments, because of different absorption coefficients. For both phantoms, the environment is perfusionless, so, for short time intervals the temperature distribution is assumed to have a shape just it is in the MCML simulations. This short time interval was assumed to have a value in between 5 – 6 minutes with the application of 7W, by looking in the change in shapes of Figure 5.3.5 D and E. When the time increases, the shape of the burn or deformations gets drifted apart from the SAR distribution. Obviously, this is the main reason why depth to width ratios of hand-fan gel phantom experiment and hand-fan MR thermometry of a gel phantom experiment differ (Table 5.5.1).

For either case (gel or tissue results), with hand-fan design or RF deliveries, depth to width ratios are less than 1. If it was 1, then the lesion is said to have perfect half - circular shape. The depth to width ratio of the SAR pattern of a single fiber was simulated as 2. Also, the MR thermometry image of single fiber excitation with same experimental setup and power levels is given in Appendix A, where, the single fiber thermal deformation map has depth to width ratio of 2.5.

In simulation results, the depth was defined as the length between the pixels with highest energy value and 10% of that energy level as one moves into the layer in horizontal axis. The width on the other hand was measured between the horizontal borders of 10% level. For RF-gel studies, regions were determined by visible molten contour borders and temperature readings ($50^{o}$C). In laser-gel studies, the borders are determined as it was in RF-gel studies, however, the temperature readings were observed at 0.6 cm posterior to the holder. $50^{o}$C value of RF-gel temperature reading at the RF-gel molten border was observed to have 5 – 10 $^{o}$C increment at the posterior probe reading in laser-gel setup, and the borders were determined accordingly. In tissue experiments, the borders were determined w.r.t. the change in contrast.

However, MR Thermometry results showed that, those borders have temperature values less than $50^{o}C$, where this value is the threshold value for lesion formation. The formed burns and molten regions were compared. Since the media were perfusionless, the comparison of simulation results with experimental results gives an insight. However, if they were not, the absorption pattern and the temperature response should not be compared.

# CHAPTER 6

## DISCUSSIONS AND CONCLUSIONS

In this preliminary work, it was shown that we are able to create lesions with a novel fiber-based laser ablation scheme, where the lesion pattern imitates the commonly used RF energy delivery techniques. To do so, multiple fiber scheme was simulated by Monte Carlo Modeling Based approach. As a starting point, 2D problem of getting a half circular (RF like) ablation zone was investigated and it was concluded that, a three – fiber orientation is enough to get RF like patterns.

No in vivo study was conducted. This can only be achieved by modifying our hand-fan design so as to be insertable through vessels. This can be succeeded by finding a way to put hand-fan design into a much smaller catheter end (by using tapered end fibers supported with scattering particles). The ultimate goal is to compare cardiac lesions for in-vivo studies with or without MR guidance, where, it can only be done by catheter approach, not by our current hand-fan design (it is not suitable for this operation). However, hand-fan design results are promising and gives an idea about the fiber orientations.

The output of the combined MCML approach and MATLAB subroutine gives 2D and 3D SAR distributions. However, there is no impulsive SAR distribution of RF ablation lesions, but, there are many temperature distribution simulations and experiment results. Considering those available data, temperature distributions and burn formations were compared. To understand the real time effect, results are supported with MR thermometry images. From the results, it is seen that the depth to width ratios of hand-fan design and RF delivery are close. The hand fan design seems to penetrate deeper. So, depth to

width ratio is greater than it is obtained with RF delivery. To obtain exact effect, the wavelength of laser system may be changed, however, whenever the depth to width ratio is smaller than or equal to 1, the lesion is said to have half – circular pattern, which is nice. Moreover, deeper temperature response of laser ablation may be used to obtain perfect transmurality, where, it cannot be achieved for some regions with RF ablation. In future works, better depth / width aspect ratio identification should be done. This will provide us more comfortable and accurate comparisons.

To summarize, the real-time MR thermometry images are consistent with local temperature measurements. In addition, the lesion patterns as determined both from thermal maps, and slices of ablated tissue are mutually consistent and in agreement with numerical simulations. The preliminary results are promising. As explained earlier, several diffusing tip designs are available. These designs diffuse light in cylindrical geometry. Besides, due to their design specifications, they cannot be directly used in place of RF probes in the treatment of AF. However, for tumor ablations, they may be quite useful. The following research should include spherical diffusing tip designs either. Spherical laser energy induced lesions as described here are deeper, potentially minimizing recurrence of AF after the treatment and may compensate the deficiencies of the RF ablation. This approach has full MR compatibility: no distortion in the phase images occurs, and real-time MR thermometry maps during the operation can easily be recorded. Efforts are under way to develop a more compact scheme; such the fibers can be packaged to 1-2 mm diameter to be inserted through blood vessels. Different orientations and fiber tips are being explored to obtain beam profiles closer to a perfect spherical distribution. Besides, with the help of MR guidance and novel catheter tracking techniques, the atrial thickness of the region of interest can be visualized. So, a variable wavelength laser system can be designed to be used safely upon ablating varying thickness of tissue.

# APPENDIX A

The Figure A1 shows the MR thermometry image of a single fiber perpendicularly exciting the gel phantom with 9W 158 seconds delivery of laser energy. The depth to width ratio of the temperature distribution of single fiber excitation inside the gel is 25 pixels/10 pixels = 2.5.

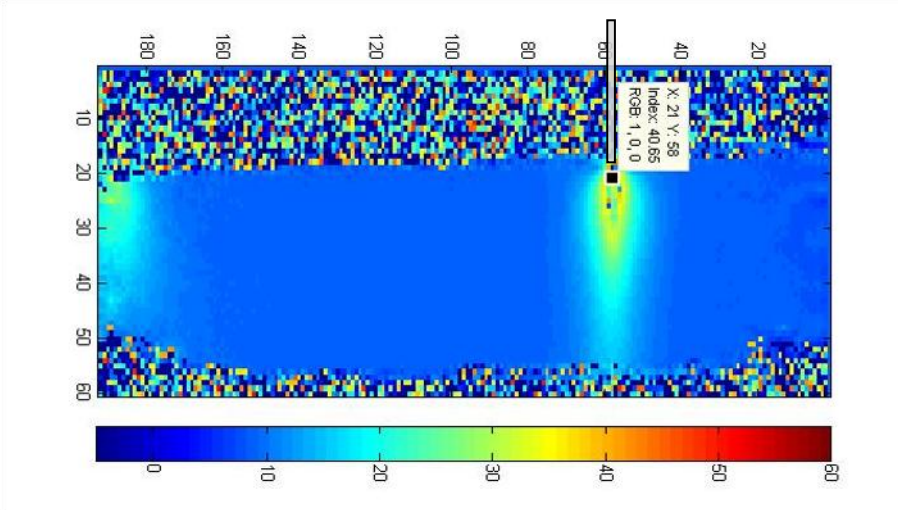


Figure A1: MR thermometry image of gel phantom with single fiber excitation (9W 158 seconds delivery).

# APPENDIX B

The Figure B1 shows the absorption coefficient ($\mu_a$) vs. wavelength graph of aorta. The graph includes the values which are obtained by using different techniques by different researchers and was compiled by Steven Jacques [54].

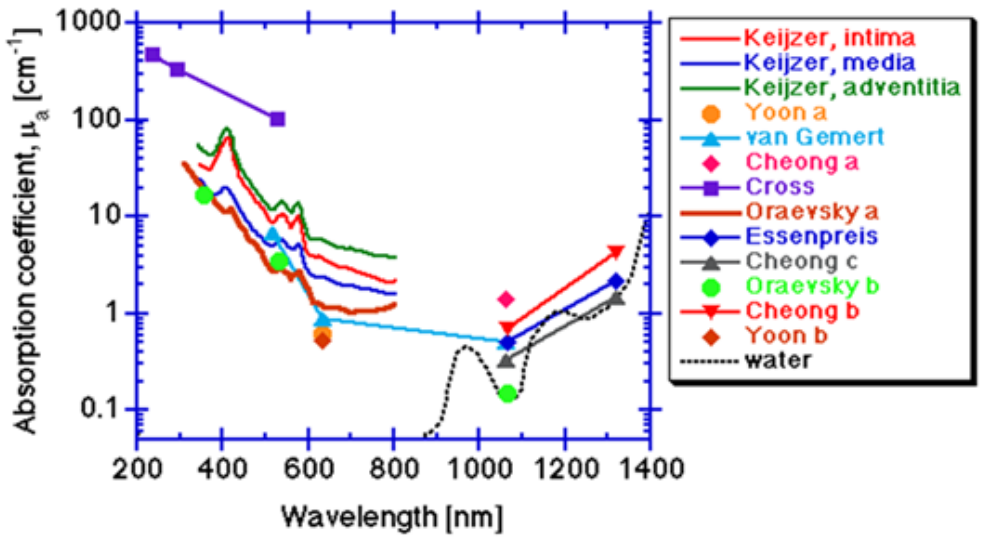


Figure B1: Absorption coefficient vs. wavelength of aorta by Steven Jacques.

# BIBLIOGRAPHY


1. Mitchell, M.A., I.D. McRury, and D.E. Haines, *Linear atrial ablations in a canine model of chronic atrial fibrillation: morphological and electrophysiological observations.* Circulation, 1998. **97**(12): p. 1176-85.
2. *Heart Rhythm Society*. Available from: <http://www.hrsonline.org/PatientInfo/HeartRhythmDisorders/AFib/>.
3. *Health System*. Available from: http://www.healthsystem.virginia.edu/Internet/afibcenter/whatis.cfm.
4. Rosamond, W., et al., *Heart disease and stroke statistics--2007 update: a report from the American Heart Association Statistics Committee and Stroke Statistics Subcommittee.* Circulation, 2007. **115**(5): p. e69-171.
5. Cox, J.L. and T.M. Sundt, 3rd, *The surgical management of atrial fibrillation.* Annu Rev Med, 1997. **48**: p. 511-23.
6. Chiappini, B., et al., *Cox/Maze III operation versus radiofrequency ablation for the surgical treatment of atrial fibrillation: a comparative study.* Ann Thorac Surg, 2004. **77**(1): p. 87-92.
7. Chiappini, B., R. Di Bartolomeo, and G. Marinelli, *Radiofrequency ablation for atrial fibrillation: different approaches.* Asian Cardiovasc Thorac Ann, 2004. **12**(3): p. 272-7.
8. Panescu, D., et al., *Three-dimensional finite element analysis of current density and temperature distributions during radio-frequency ablation.* IEEE Trans Biomed Eng, 1995. **42**(9): p. 879-90.
9. Pichardo, S. and K. Hynynen, *Circumferential lesion formation around the pulmonary veins in the left atrium with focused ultrasound using a 2D-array endoesophageal device: a numerical study.* Phys Med Biol, 2007. **52**(16): p. 4923-42.
10. Thomas, S.P., et al., *Production of narrow but deep lesions suitable for ablation of atrial fibrillation using a saline-cooled narrow beam Nd:YAG laser catheter.* Lasers Surg Med, 2001. **28**(4): p. 375-80.
11. Williams, M.R., et al., *Alternative energy sources for surgical atrial ablation.* J Card Surg, 2004. **19**(3): p. 201-6.
12. Cox, J.L., *Cardiac surgery for arrhythmias.* J Cardiovasc Electrophysiol, 2004. **15**(2): p. 250-62.
13. Berjano, E.J., *Theoretical modeling for radiofrequency ablation: state-of-the-art and challenges for the future.* Biomed Eng Online, 2006. **5**: p. 24.
14. Gazelle, G.S., et al., *Tumor ablation with radio-frequency energy.* Radiology, 2000. **217**(3): p. 633-46.
15. Jain, M.K. and P.D. Wolf, *In vitro temperature map of cardiac ablation demonstrates the effect of flow on lesion development.* Ann Biomed Eng, 2000. **28**(9): p. 1066-74.

16. Jain, M.K. and P.D. Wolf, *A three-dimensional finite element model of radiofrequency ablation with blood flow and its experimental validation.* Ann Biomed Eng, 2000. **28**(9): p. 1075-84.
17. Nath, S., et al., *Cellular electrophysiological effects of hyperthermia on isolated guinea pig papillary muscle. Implications for catheter ablation.* Circulation, 1993. **88**(4 Pt 1): p. 1826-31.
18. Thomas, S.P., et al., *Comparison of epicardial and endocardial linear ablation using handheld probes.* Ann Thorac Surg, 2003. **75**(2): p. 543-8.
19. Berjano, E.J., et al., *Improved perfusion system for bipolar radiofrequency ablation of liver: preliminary findings from a computer modeling study.* Physiol Meas, 2006. **27**(10): p. N55-66.
20. Berjano, E.J. and F. Hornero, *Thermal-electrical modeling for epicardial atrial radiofrequency ablation.* IEEE Trans Biomed Eng, 2004. **51**(8): p. 1348-57.
21. Wiley, J.D. and J.G. Webster, *Analysis and control of the current distribution under circular dispersive electrodes.* IEEE Trans Biomed Eng, 1982. **29**(5): p. 381-5.
22. Gopalakrishnan, J., *A mathematical model for irrigated epicardial radiofrequency ablation.* Ann Biomed Eng, 2002. **30**(7): p. 884-93.
23. Labonte, S., *Numerical model for radio-frequency ablation of the endocardium and its experimental validation.* IEEE Trans Biomed Eng, 1994. **41**(2): p. 108-15.
24. Chang, I.A. and U.D. Nguyen, *Thermal modeling of lesion growth with radiofrequency ablation devices.* Biomed Eng Online, 2004. **3**(1): p. 27.
25. Nakagawa, H., et al., *Inverse relationship between electrode size and lesion size during radiofrequency ablation with active electrode cooling.* Circulation, 1998. **98**(5): p. 458-65.
26. Niemz, M.H., *Laser-tissue interactions : fundamentals and applications*. 3rd, enlarged ed. Biological and medical physics, biomedical engineering,. 2004, Berlin ; New York: Springer. xvi, 305 p.
27. Ishimaru, A., *Diffusion of Light in Turbid Material.* Applied Optics, 1989. **28**(12): p. 2210-2215.
28. Welch, A.J., *The Thermal Response of Laser Irradiated Tissue.* Ieee Journal of Quantum Electronics, 1984. **20**(12): p. 1471-1481.
29. Bohren, C.F. and D.R. Huffman, *Absorption and scattering of light by small particles*. 1983, New York: Wiley. xiv, 530 p.
30. Motamedi, M., et al., *Light and Temperature Distribution in Laser Irradiated Tissue - the Influence of Anisotropic Scattering and Refractive-Index.* Applied Optics, 1989. **28**(12): p. 2230-2237.
31. Lardo, A.C., et al., *Magnetic resonance guided radiofrequency ablation: Visualization and temporal characterization of thermal lesions.* Circulation, 1998. **98**(17): p. 644-644.
32. Lardo, A.C., et al., *Magnetic resonance guided radiofrequency ablation: Creation and visualization of cardiac lesions.* Medical Image

Computing and Computer-Assisted Intervention - Miccai'98, 1998. **1496**: p. 189-196.
33. Susil, R.C., et al., *Multifunctional interventional devices for MRI: a combined electrophysiology/MRI catheter.* Magn Reson Med, 2002. **47**(3): p. 594-600.
34. Ashok Gowda, R.J.M., MArc Gelnett, Matthew Fox, *Light Diffusing Tip*. 2008, Biotex, Inc. Houston, TX USA.
35. Easley, J.C., *Wide Angle Light Diffusing Optical Fiber Tip*. 2004, Syntec, Inc., Winfield, MO (US).
36. Daniel R. Dorion, S.Y., *Diffusing Tip For Optical Fibers*. 1993, PDT Systems, Inc., Goleta, Calif.: US.
37. Chapman, J.G., *Diffusive Optical Fibre Termination*. 1985, Quentron Optics Pty Ltd (South - Australia).
38. Fried, N.M., et al., *Linear lesions in myocardium created by Nd : YAG laser using diffusing optical fibers: In vitro and in vivo results.* Lasers in Surgery and Medicine, 2000. **27**(4): p. 295-304.
39. Sato, S., et al., *Nanosecond, high-intensity pulsed laser ablation of myocardium tissue at the ultraviolet, visible, and near-infrared wavelengths: in-vitro study.* Lasers Surg Med, 2001. **29**(5): p. 464-73.
40. Peters, D.C., et al., *Detection of pulmonary vein and left atrial scar after catheter ablation with three-dimensional navigator-gated delayed enhancement MR imaging: Initial experience.* Radiology, 2007. **243**(3): p. 690-695.
41. Kettenbach, J., et al., *Real-time monitoring and analysis of MR-guided laser ablation in an open-configuration MR-system.* Lasers in Surgery: Advanced Characterization, Therapeutics, and Systems Viii, Proceedings Of, 1998. **3245**: p. 98-108 460.
42. Cheong, W.F., S.A. Prahl, and A.J. Welch, *A Review of the Optical-Properties of Biological Tissues.* Ieee Journal of Quantum Electronics, 1990. **26**(12): p. 2166-2185.
43. Keijzer, M. and A.J. Hermans, *Light Diffusion in Stochastically Perturbed Media.* Journal of the Optical Society of America a-Optics Image Science and Vision, 1993. **10**(11): p. 2346-2353.
44. Keijzer, M., et al., *Fluorescence Spectroscopy of Turbid Media - Autofluorescence of the Human Aorta.* Applied Optics, 1989. **28**(20): p. 4286-4292.
45. Bolin, F.P., et al., *Refractive-Index of Some Mammalian-Tissues Using a Fiber Optic Cladding Method.* Applied Optics, 1989. **28**(12): p. 2297-2303.
46. Keijzer, M., W.M. Star, and P.R.M. Storchi, *Optical Diffusion in Layered Media.* Applied Optics, 1988. **27**(9): p. 1820-1824.
47. van Gemert, M.J., et al., *Optical properties of human blood vessel wall and plaque.* Lasers Surg Med, 1985. **5**(3): p. 235-7.

48. Wang, L.H., S.L. Jacques, and L.Q. Zheng, *Mcml - Monte-Carlo Modeling of Light Transport in Multilayered Tissues.* Computer Methods and Programs in Biomedicine, 1995. **47**(2): p. 131-146.
49. Ma, N., X. Gao, and X.X. Zhang, *Two-layer simulation model of laser-induced interstitial thermo-therapy.* Lasers in Medical Science, 2004. **18**(4): p. 184-189.
50. Kaufmann, R. and R. Hibst, *Pulsed Erbium:YAG laser ablation in cutaneous surgery.* Lasers in Surgery and Medicine, 1996. **19**(3): p. 324-330.
51. Williams, M.R., et al., *Application of microwave energy in cardiac tissue ablation: From in vitro analyses to clinical use.* Annals of Thoracic Surgery, 2002. **74**(5): p. 1500-1509.
52. Panescu, D., et al., *Optimisation of transcutaneous cardiac pacing by three-dimensional finite element modelling of the human thorax.* Med Biol Eng Comput, 1995. **33**(6): p. 769-75.
53. Peters, R.D., R.S. Hinks, and R.M. Henkelman, *Ex vivo tissue-type independence in proton-resonance frequency shift MR thermometry.* Magnetic Resonance in Medicine, 1998. **40**(3): p. 454-459.
54. Jacques, Steven, *Optical Properties of Aorta*. Available from: http://omlc.ogi.edu/spectra/aorta/index.html